

Particle acceleration at recollimation shocks in sub-relativistic jets

A model for jets in Seyfert Galaxies, Microquasars and Protostellar Systems

E. Peretti^{1,2,*}, E. Amato¹, S. S. Cerri³, G. Morlino¹, L.P. Pullano^{1,4}, and S. Recchia^{1,5}

¹ INAF, Istituto Nazionale di Astrofisica, Osservatorio Astronomico di Arcetri, Largo E. Fermi 5, 50125 Florence, Italy

² Astroparticule et Cosmologie, Université Paris Cité, 10 Rue Alice Domon et Léonie Duquet, F-75013 Paris, France

³ Université Côte d'Azur, Observatoire de la Côte d'Azur, CNRS, Laboratoire Lagrange, Bd de l'Observatoire, CS 34229, 06304 Nice cedex 4, France

⁴ University of Pisa, Lungarno Antonio Pacinotti, 43, 56126 Pisa, Italy

⁵ Institute of Nuclear Physics Polish Academy of Sciences, PL-31342 IFJ-PAN, Krakow, Poland

Received XXX, XXX; accepted XXX, XXX

ABSTRACT

Context. Growing observational evidence suggests that sub-relativistic astrophysical jets may accelerate particles at slowly evolving standing shocks. Recollimation shocks are expected to develop when jets expand in dense environments; their formation may be mediated by the pressure of the cocoon surrounding the jet, while remaining compatible with a quasi-stationary behavior. Despite their high inclination relative to the jet axis, such shocks can be strong and enable efficient particle acceleration.

Aims. The aim of this work is to improve the general understanding of particle acceleration via diffusive shock acceleration at recollimation shocks by developing a versatile modeling framework applicable to different classes of astrophysical jets, including Seyfert galaxies, microquasars, and protostellar systems.

Methods. We extend an analytic jet hydrodynamics model previously introduced in the literature to the sub-relativistic regime and use it to identify the expected locations of the recollimation shock and the jet head. Within this framework, we formulate a semi-analytic acceleration and transport model for particles injected at the recollimation shock via diffusive shock acceleration.

Results. By solving the space-dependent transport equation, we obtain particle distributions and spectra along the jet, as well as robust predictions for the maximum energies achievable as a function of the intrinsic properties of the system and the source class.

Conclusions. Our results indicate that recollimation shocks may play a central role in particle acceleration in sub-relativistic jets. In Seyfert galaxies, such shocks may accelerate particles from PeV up to EeV energies, while in microquasars and protostellar jets maximum energies of tens of PeV and up to TeV are expected, respectively. Protons escaping the jets may diffuse through the cocoon, leading to possible hadronic signatures.

Key words. particle acceleration – jets – microquasars – active galaxies – protostars

1. Introduction

Astrophysical systems can produce collimated outflows, or jets, across a wide range of power and spatial scales. The acceleration and collimation of these jets can result from different physical mechanisms, including geometric collimation by dense ambient material, magnetic tension, recollimation shocks of different nature or magneto-rotational effects. The extraction of rotational energy from compact objects (Penrose 1969; Blandford & Znajek 1977) and magneto-centrifugal disk winds (Blandford & Payne 1982) have long been considered among the most efficient launching mechanisms of jets. Early magneto-hydrodynamic (MHD) simulations demonstrated the feasibility of jet formation in magnetized disks (Shibata & Uchida 1986), and more recent general relativistic MHD studies have shown that, in magnetically arrested disks, the outflow luminosity can exceed the accretion power in agreement with the energy extraction resulting from the Blandford–Znajek process (Tchekhovskoy et al. 2011).

As soon as jets were understood to be highly supersonic, the presence of strong shocks was promptly postulated and, consequently, diffusive shock acceleration (DSA) was soon considered as a viable mechanism to accelerate particles in these ob-

jects. Indeed, pioneering theoretical works on particle acceleration and radio emission established the foundations for interpreting jet phenomenology (Blandford & Rees 1974; Scheuer 1974; Blandford & Rees 1978; Blandford & Königl 1979). The first hydrodynamic simulations then clarified the basic structure of supersonic jets and characterized the shocked environments, as well as the formation of wide regions—typically referred to as cocoons—surrounding the jets themselves (Norman et al. 1982). The propagation of shocks in jets has been proposed as a key ingredient in explaining spectral evolution in jets of active galactic nuclei (AGN), such as blazars (Marscher & Gear 1985), while subsequent relativistic simulations examined the role of external pressure gradients (Daly & Marscher 1988), jet confinement induced by the cocoon (Begelman & Cioffi 1989), and the formation of standing shocks (Gomez et al. 1995; Gómez & Marscher 2000). Relativistic effects such as superluminal motion (Gómez et al. 1997) and the emergence of shock-induced knots (Komisarov & Falle 1997) were naturally reproduced. Analytical treatments of jet expansion in active galaxies (Kaiser & Alexander 1997) and time-dependent MHD simulations (Ouyed & Pudritz 1999) further constrained jet stability, while non-relativistic shocks triggered by Kelvin–Helmholtz instabilities were shown to efficiently accelerate electrons (Micono et al. 1999).

* enrico.peretti.science@gmail.com

Important progress on the jet dynamics has been achieved also through analytic studies. In particular, analytic models of jet–cocoon systems indicated that the degree of collimation depends sensibly on the ambient conditions, predicting either tightly collimated or freely expanding outflows (Krause 2003; Bromberg et al. 2011). This behavior was found to be consistent with 2D relativistic MHD simulations, which found that axial magnetic fields strengthen recollimation shocks, whereas predominantly toroidal fields tend to weaken them (Mizuno et al. 2015). Three-dimensional MHD simulations have shown that kink instabilities can generate shocks and produce the knotty structures observed in many jets (Moll et al. 2008). In addition, when radiative losses were included, simulations also showed pronounced flow focusing downstream of the recollimation region (Bodo & Tavecchio 2018). Interestingly, interactions between jets and embedded obstacles were suggested to locally boost non-thermal emission (Bosch-Ramon 2015).

Collimated jets in astrophysical systems have been observed over a wide range of speeds, from 10^2 km s^{-1} in the case of protostars, up to Lorentz factors $\Gamma \gg 1$ in the case of AGN and gamma-ray bursts. However, relativistic shocks are known to be inefficient in accelerating particles, hence here we focus on shocks from non-relativistic jets, and we limit our discussion to those sources featuring bulk Lorentz factors $\Gamma \lesssim 2$. These are mainly found in the objects presented below.

Microquasars: Powered by the accretion of a stellar-mass compact object from a companion star, microquasars are the prototypical Galactic objects where jets are observed with both mildly relativistic and highly relativistic velocities. Apparent superluminal motions were first identified in these systems by Mirabel & Rodríguez (1994, 1998). Their non-thermal emission has been interpreted through various leptonic (Band & Grindlay 1986; Atoyan & Aharonian 1999; Romero et al. 2002) and hadronic scenarios (Romero et al. 2003). Several models address cosmic-ray (CR) production in microquasar environments (Heinz & Sunyaev 2002). Multi-zone leptonic and lepto-hadronic frameworks have been applied to a range of sources (Bosch-Ramon & Paredes 2004a,b; Markoff et al. 2005; Bosch-Ramon et al. 2005; Romero & Vila 2008; Vila & Romero 2010; Sudoh et al. 2020; Kimura et al. 2020; Kantzas et al. 2021; Khangulyan et al. 2024; Wan et al. 2025). Hydrodynamic simulations have examined shock formation (bow, termination, and recollimation) (Bordas et al. 2009) and jet propagation in complex environments (Bosch-Ramon et al. 2011). High-energy variability, absorption, and pair production have been extensively studied, particularly in Cygnus X-3 (Dubus et al. 2010; Zdziarski et al. 2012; Cerutti et al. 2011; Tavani et al. 2009; Fermi LAT Collaboration et al. 2009). In these systems, stellar winds may trigger jet launching even in the absence of a stable accretion disk (Barkov & Khangulyan 2012).

SS433 is another Galactic microquasar featuring extremely interesting and complex features. Besides the mildly relativistic jet resulting from a super-Eddington accreting stellar-mass compact object, it is characterized by a wide opening angle mildly relativistic outflow typical of ultra luminous X-ray sources (Middleton et al. 2021). Such observations led to recent interesting hypotheses on the nature of the surrounding nebula, W50, as the result of superposition of a disc wind interacting with the jet (Churazov et al. 2024). This interpretation seems to be supported by diffuse X-ray emission observed by e-Rosita (Sunyaev et al. 2025). However, the nature of the SS433/W50 nebula is still highly uncertain. Intermittent jet activity has also

been suggested for SS433 (Goodall et al. 2011), whose morphology has also been reproduced through precessing-jet simulations (Monceau-Baroux et al. 2014) and analytic descriptions of recollimation shocks (Yoon et al. 2016). MHD simulations of the SS433/W50 system have also reproduced the observed nebular structure (Ohmura et al. 2021).

Interestingly, microquasars have been recently detected at very high energies (100 GeV - 100 TeV) by HAWC and HESS (Abeysekara et al. 2018; H. E. S. S. Collaboration et al. 2024; Acharyya et al. 2025), and by LHAASO up to hundreds of TeV (Lhaaso Collaboration et al. 2025), thereby suggesting that they are Galactic PeV accelerators. In addition, X-ray observations of SS433 provided further support to the presence of a strong recollimation shock (Tsuji et al. 2025). These objects were already proposed to contribute to Galactic CRs through standard proton (Romero et al. 2003) or neutron escape (Escobar et al. 2021, 2022). However, the above-mentioned recent observational evidence in the TeV domain, stimulated novel investigations. Microquasar jets (Abaroa et al. 2024; Bykov et al. 2025) as well as super-Eddington outflows have been proposed as potential Galactic PeVatrons (Peretti et al. 2025b). The contribution of microquasars to the Galactic CR population has been re-examined in several recent works (Peretti et al. 2025b; Wang et al. 2025; Zhang et al. 2025; Kaci et al. 2025). Finally, the remnants of microquasars have also been proposed to be some of the extended unidentified LHAASO sources (Abaroa et al. 2026).

Active galaxies: Launched from the nearest neighborhoods of supermassive black holes, mildly relativistic and Newtonian outflows are observed in several AGN (Veilleux et al. 2005). Examples include Seyfert galaxies such as NGC 1068 (Galimore et al. 1996b,a; Lenain et al. 2010; Salvatore et al. 2024), NGC 4151 (Ulvestad et al. 2005; Williams et al. 2017) and NGC 6764 (Kharb et al. 2010), where the jets display velocities in the range $\sim 0.01 - 0.1c$ and possibly also evidence of precession or kinks. Jet-driven acceleration of molecular gas to several hundred km s^{-1} has been reported in IC 5063 (Tadhunter et al. 2014). Recollimation shocks have also been invoked to explain non-thermal components in narrow-line Seyfert 1 jets (Doi et al. 2018; Hada et al. 2018), while simulations of non-relativistic AGN jets have explored cocoon formation (Ohmura et al. 2020). Interestingly, particle acceleration may also take place in backflows surrounding relativistic jets and achieve the highest energies in the cosmic-ray spectrum (Matthews et al. 2019). Besides their jetted activity, also non-jetted AGN can power wide opening angle winds reaching mildly relativistic velocities where particle acceleration up to the ultra-high energy domain has been proposed to take place (Wang & Loeb 2017; Peretti et al. 2023; Ehlert et al. 2025; Peretti et al. 2025a; Le Nagat Neher et al. 2026).

Protostellar jets: The possibility that young stellar objects, or protostars, could launch fast and collimated jets followed pioneering works on nebulous objects observed around young stars (Herbig 1951; Haro 1952). Protostellar jets represent indeed another class of non-relativistic collimated outflows that, different from the previous cases of microquasars and AGN, do not typically exceed velocities of $\sim 10^3 \text{ km s}^{-1}$. Early works on Herbig–Haro (HH) systems examined their dynamics and the impact of strong radiative cooling (Blondin et al. 1989). Observations of synchrotron emission in T Tauri jets suggest the presence of ordered magnetic fields that may assist collimation (Ray et al. 1997). Jets launched by young stellar objects are

expected to play an important role in angular momentum regulation (Konigl & Pudritz 2000). Radio surveys have established their extension up to parsec scales (Reipurth et al. 2004). High-energy emission has been modeled through leptonic and hadronic processes (Araudo et al. 2007), and numerical simulations have investigated the variability of radiative HH jets (Raga et al. 2007). Massive protostellar jets may produce gamma rays through particle acceleration at their terminal and reverse shocks (Bosch-Ramon et al. 2010). Evidence for efficient acceleration includes high ionization rates (Padovani et al. 2015), radio signatures compatible with diffusive shock acceleration (Rodríguez-Kamenetzky et al. 2016), and observational hints of recollimation shocks (Rodríguez-Kamenetzky et al. 2017; Carrasco-González et al. 2021). Particle acceleration at protostellar jet heads has been studied in detail (Araudo et al. 2021), and recent gamma-ray detections of protostellar systems further support this picture (Yan et al. 2022; Yang et al. 2023; de Oña Wilhelmi et al. 2023).

Despite great progress in our understanding of jet dynamics and radiation, our understanding of particle acceleration in such systems is still poor. This gap between jet dynamics and multi-messenger radiation is indeed the subject of the present paper. In particular, in this work, we develop a model of DSA at recollimation shocks induced by cocoons in the context of sub-relativistic jets. This is performed in the context of an extension of the analytic hydrodynamic framework developed by Bromberg et al. (2011). The paper is organized as follows. Section 2 is devoted to the jet structure and evolution. In Section 3 we describe the particle acceleration model and in Section 4 we present our results focusing, in particular, on the maximum energy for the accelerated particles. We discuss the limitations of our model and future prospects in Section 5. We finally draw our conclusions in Section 6.

2. The Jet-cocoon system

Collimated jets launched by compact objects are characterized by complex dynamics regulated by the interaction with the surrounding medium. In particular, when a jet is launched with supersonic velocity, it develops a terminal region known as *jet head*. Such a jet head is composed by a forward shock, which separates the undisturbed external medium from the shocked one, a contact discontinuity, which sets the separation between the shocked ambient medium and the shocked jet material, and a reverse shock, where the high velocity jet plasma is shocked. The shocked jet material and the shocked ambient medium typically flow sideways with respect to the jet axis and fill a hot and high-pressure cocoon. In particular, inner and outer cocoons are inflated respectively by the shocked jet material and the shocked ambient material. The cocoon surrounds the jet and can contribute to confine its opening angle beyond a certain distance from the central engine. In particular, if the component of the ram pressure perpendicular to the jet axis falls below the thermal pressure in the cocoon, a recollimation shock forms and the jet is forced to change its geometry from conical to cylindrical. A sketch of the jet-cocoon system is shown in Figure 1.

Newtonian jets from microquasars, AGN and some protostars are expected to be characterized by a plasma density smaller than the one of the medium in which they are expanding. This results in a dominant role played by the cocoon in the jet collimation, and consequently leads to the formation of a recollimation shock (Bromberg et al. 2011). Recollimation shocks are generally characterized by a certain angle between the fluid

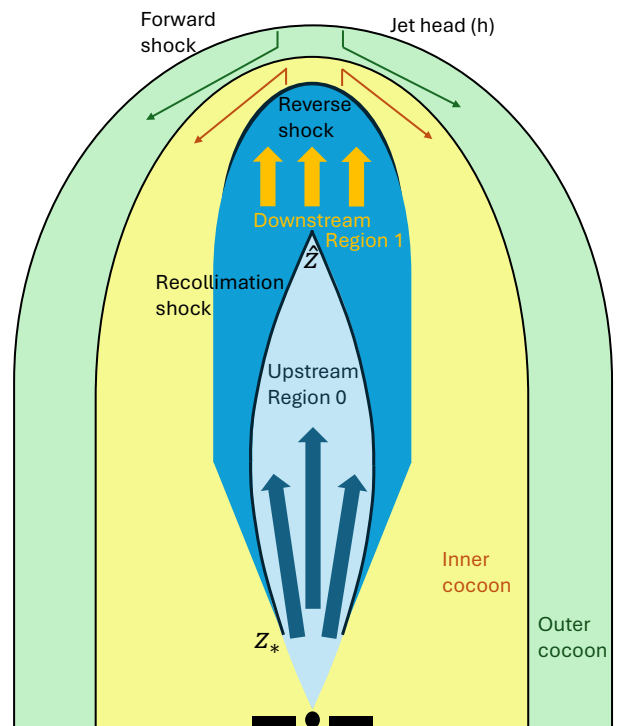


Fig. 1. Sketch illustrating the jet-cocoon system. Particles are accelerated at the recollimation shock and then advected in the jet. The jet material that passes through the reverse shock fills the inner cocoon (yellow area), while the external medium reached by the jet head and, laterally, by the cocoon surface, is swept-up and accumulated in the outer cocoon (green area).

motion and the normal to the shock. In other words, they are oblique with respect to the flow propagation direction. Nevertheless, they can be strong enough to efficiently accelerate particles as we will show below.

Although astrophysical jets close to their central engine are expected to be magnetically dominated and with strong helical magnetic fields that help in the collimation, we are interested in the properties of these systems at larger scales. At large distance from the central engine jets are expected to become kinetically dominated because of the rapid dissipation of Poynting flux (see e.g. Giannios & Spruit 2006). In general, the ram pressure is expected to dominate over the thermal pressure which, in turn, is expected to be larger than the magnetic pressure. This makes the assumption of a pure hydrodynamic model qualitatively justified. In this context, we develop an analytic hydrodynamic model for the sub-relativistic jet-cocoon system inspired by the formalism of Bromberg et al. (2011) (see also Krause 2003).

2.1. Jump conditions at the recollimation shock

Recollimation shocks are expected to be elongated, and to form cusps along the jet axis. Consequently, the upstream plasma impacts the shock at a certain angle with respect to the shock-normal. After crossing the shock, only the velocity component parallel to the shock-normal is reduced, while the tangential component remains unaltered. As a consequence, the plasma flow is deflected approximately parallel to the jet axis in the downstream—hence, the name recollimation shock. Thus, the Rankine-Hugoniot jump conditions only hold for the normal component of the flow u , hereafter denoted by a subscript n . This

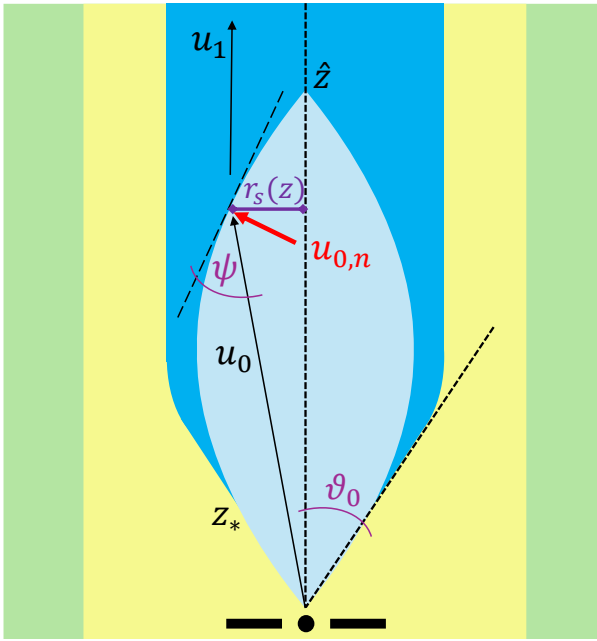


Fig. 2. Sketch illustrating the recollimation shock geometry. The upstream fluid with velocity u_0 impacts the shock with angle ψ and is deflected along the jet axis. The component normal to the shock of the upstream velocity is $u_{0,n}$. The downstream plasma speed is u_1 . The shock radius, r_s , is the radius of the shock which approximately coincides with the jet radius at $\hat{z}/2$. The recollimation shock forms at z_* .

results in the following definition for the compression ratio

$$r = \frac{u_{0,n}}{u_{1,n}} = \frac{(\gamma + 1)M_{0,n}^2}{(\gamma - 1)M_{0,n}^2 + 2} \quad (1)$$

where the subscript 0 (1) indicates that the quantity is computed in the upstream (downstream), γ is the adiabatic index of the gas, and $M_{0,n}$ is the upstream Mach number associated with the normal component of the flow. Mach numbers of mildly relativistic and sub-relativistic jets typically range from a few up to a few tens. This is enough to make the shock an efficient accelerator, while, as we discuss in Section 5, it might be not enough to guarantee spectra as hard as $\sim E^{-2}$.

The inclination of the recollimation shock is extremely relevant for the characterization of the accelerator properties as well as the jet structure. In fact, higher inclinations between the shock normal and the velocity vector result in lower acceleration efficiency for the accelerated particles, because the pressure of accelerated particles is expected to be a fraction of the ram pressure component normal to the shock. Similarly, also the jet thermal pressure downstream of the shock, P_1 , strongly depends on the angle. From the pressure jump condition one can express such pressure as

$$P_1 = \frac{(r - 1)}{r} \sin^2 \psi \rho_0 u_0^2 = k_p \rho_1 u_1^2, \quad (2)$$

where ψ is the angle between the shock surface and the upstream velocity vector (see Figure 2), $\rho_{0(1)}$ represents the upstream (downstream) density, and k_p is the thermal-to-ram pressure ratio in the downstream plasma, which can be expressed as:

$$k_p = \frac{r - 1}{1 + r^2 \cot^2 \psi}. \quad (3)$$

We parametrize with k_p the impact of the shock inclination on the downstream pressure reminding the reader that typically it

can range from 3 in the case of strong shock and large inclination angle (i.e. $\psi \approx 90^\circ$), down to $k_p \ll 1$ for $\psi \ll 90^\circ$. It is worth noticing that the strength of the reverse shock at the jet head is linked to the recollimation shock inclination. Indeed, using Equation (2) we can express the Mach number at the reverse shock as:

$$M_1 = \frac{u_1}{c_{s,1}} = \frac{1}{\sqrt{\gamma k_p}} \quad (4)$$

such that small ψ results in a strong reverse shock, and *vice-versa*. In general we expect $k_p \ll 1$ and the reverse shock to be strong.

2.2. Jet characterization

The motion of the jet head is regulated by the pressure balance between the jet (ram pressure and thermal pressure) and the ram pressure of the external medium

$$\rho_1 (u_1 - v_h)^2 + P_1 = \rho_A v_h^2 \quad (5)$$

where $\rho_A = n_A m_p$ is the density of the external medium and v_h is the velocity of the jet head. In the latter equation we neglected the role played by the thermal pressure of the external medium on the right hand side. Adopting the same formalism of Bromberg et al. (2011) we define \tilde{L} as

$$\tilde{L}(t) = \frac{\rho_1}{\rho_A} = \frac{2L_j}{\rho_A u_1^3 \Sigma_1(t) \zeta}, \quad (6)$$

where L_j is the jet kinetic luminosity, Σ_1 is the jet section after the recollimation shock. ζ is a parameter of order unity that encompasses the normalized contribution of ram pressure and thermal pressure to the total jet kinetic power

$$L_j = \Sigma_0 \frac{1}{2} \rho_0 u_0^3 = \Sigma_1 \left[\frac{1}{2} \rho_1 u_1^3 + \frac{\gamma}{(\gamma - 1)} P_1 u_1 \right] = \Sigma_1 \frac{1}{2} \rho_1 u_1^3 \zeta, \quad (7)$$

so that $\zeta = [1 + 2\gamma k_p / (\gamma - 1)]$. For $\gamma = 5/3$ depending on the recollimation shock strength it is possible to see that $1 \leq \zeta \leq r^2$, and $\zeta \approx 1$ when $k_p \ll 1$.

By solving Equation (5) with the use of Equation (2), we find the following expression for the jet head speed

$$v_h(t) = u_1 \frac{(1 + k_p)}{1 + \sqrt{1 + (1 + k_p)(\tilde{L}^{-1}(t) - 1)}}. \quad (8)$$

We notice that for $k_p \ll 1$ we recover the solution from Bromberg et al. (2011) for a sub-relativistic jet, i.e. $v_h(t) \approx u_1 / (1 + \tilde{L}^{-1/2})$. In such a limit, the expression for v_h is valid for all values of \tilde{L} while, for a non-negligible k_p , the existence of a physical solution requires $\tilde{L} \leq (1 + k_p) / k_p$.

In the limit $\tilde{L} \ll 1$ the head velocity reads

$$v_h(t) \sim u_1 \tilde{L}^{1/2}(t) \sqrt{1 + k_p}. \quad (9)$$

2.2.1. Cocoon

If strong shock conditions are realized at the reverse shock, the hot shocked gas flows orthogonally to the jet axis and leaves the jet head feeding the inner cocoon, namely the region of shocked jet material that surrounds the whole jet structure from the head to the central engine. The inner cocoon is then surrounded by

the outer cocoon, namely the ambient gas that has been swept-up and shocked by the forward shock at the jet head, or possibly also by the lateral expansion of the cocoon itself.

The energy injected by the jet in the cocoon can be parametrized as

$$E_c \approx \eta L_j t, \quad (10)$$

where $\eta < 1$ is an efficiency parameter accounting for the conversion of jet kinetic energy into pressure at the reverse shock and the amount of energy, E_j , still stored in the jet. While such energy can be relevant at early times, when the cocoon is yet to be formed, at later times, it becomes subdominant because $E_j/E_c = (L_j z_h/u_1)/(\eta L_j t) \approx v_h/(\eta u_1)$ which is $\ll 1$ if $\tilde{L} \ll 1$ (see Equation (9)).

The vertical expansion of the cocoon is set by the motion of the jet head along the jet axis, while the lateral expansion velocity, v_c , is set by the pressure balance between the external ram pressure and the pressure in the cocoon, so that one has $v_c(t) = \sqrt{P_c(t)/\rho_A}$. By approximating the cocoon as a cylinder, it is possible to estimate its volume as

$$V_c(t) = z_h(t)\pi R_c^2(t) = \pi C B^2 t^{\alpha+2\beta} = \pi v_h(t)v_c^2(t)t^3/\alpha\beta^2, \quad (11)$$

where we assumed a self-similar scaling for the cocoon height— $z_h(t) = \int dt v_h(t) = C t^\alpha$ —and radius— $R_c(t) = \int dt v_c(t) = B t^\beta$. C and B are constants to be determined, while α and β are self-similar indexes. By using Equations (10), (11) and (8), the pressure in the cocoon can be expressed as

$$\begin{aligned} P_c(t) &= (\gamma - 1) \frac{E_c(t)}{V_c(t)} = \\ &= \frac{\left[1 + \sqrt{1 + (1 + k_p)(\tilde{L}^{-1}(t) - 1)}\right]^{1/2}}{t} \left[\frac{(\gamma - 1)\eta L_j \rho_A \alpha \beta^2}{\pi u_1 (1 + k_p)} \right]^{1/2} \\ &\xrightarrow{\tilde{L} \ll 1} \frac{\tilde{L}^{-1/4}(t)}{t} \left[\frac{L_j \rho_A}{3\pi u_1} \right]^{1/2} \left[\frac{3(\gamma - 1)\eta \alpha \beta^2}{(1 + k_p)^{1/2}} \right]^{1/2} \end{aligned} \quad (12)$$

where the latter expression is obtained for $\tilde{L} \ll 1$. We notice that our result is equivalent to Equation (7) from Bromberg et al. (2011). This is especially clear in the limit $\tilde{L} \ll 1$.

2.2.2. Recollimation shock

The recollimation shock is located where the upstream ram pressure normal to the shock surface matches the pressure in the cocoon

$$\rho_0 u_{0,n}^2 = \rho_0 u_0^2 \sin^2 \psi \approx P_c. \quad (14)$$

As the upstream plasma is freely expanding with a certain opening angle θ_0 , the ram pressure, $\rho_0 u_0^2$, is expected to drop approximately as z^{-2} . Following Bromberg et al. (2011), for small angles ψ , the following relation holds

$$\sin \psi \approx \frac{r_s(z)}{z} - \frac{dr_s}{dz}, \quad (15)$$

where z measures the distance from the engine along the jet, while r_s represents the shock radius (see Figure 2). Substituting the latter result into Equation (14) allows one to obtain an analytic solution of the first order differential equation for r_s , which reads

$$r_s(z) = \theta_0(1 + A z_*)z - A\theta_0 z^2, \quad (16)$$

where $A = \sqrt{P_c(t)\pi u_0/[2L_j]}$ and z_* is the location, typically closer to the central engine, where the recollimation shock forms. At this point it is possible to obtain the general expression for the angle ψ , $\sin \psi(z) = A\theta_0 z$, implying that ψ ranges approximately between $\theta_0/2$ and θ_0 . The recollimation shock has a parabolic shape as shown in Figure 2. By setting $r_s = 0$ and $dr_s/dz = 0$ one can find, respectively, the position $\hat{z} = A^{-1} + z_* \approx A^{-1}$, where the recollimation shock converges on the jet axis, and the position $\bar{z} = \hat{z}/2$, where the shock surface is parallel to the jet axis and the jet changes from a conical to a cylindrical shape. The jet section beyond the recollimation shock can now easily be computed as

$$\Sigma_1(t) = \pi r_s^2(\bar{z}) = \pi \left(\frac{\hat{z}}{2}\right)^2 \theta_0^2 \approx \frac{L_j \theta_0^2}{2P_c(t)u_0}. \quad (17)$$

2.2.3. Relevant scalings

As the main focus of this work is on sub-relativistic and mildly relativistic jets we proceed in this section under the physically motivated assumption of $\tilde{L} \ll 1$.

Substituting Equations (12)–(17) in Equation (6) it is possible to obtain the temporal evolution of \tilde{L}

$$\tilde{L}(t) = \frac{4}{u_1^2} L_j^{2/5} \theta_0^{-8/5} \rho_A^{-2/5} t^{-4/5} \left[\frac{(\gamma - 1)\eta \alpha \beta^2 (u_0/u_1)^2}{2\pi \zeta^2 (1 + k_p)^{1/2}} \right]^{2/5}. \quad (18)$$

Plugging the latter result in Equation (12) the cocoon pressure reads

$$P_c(t) = L_j^{2/5} \theta_0^{2/5} \rho_A^{3/5} t^{-4/5} \left[\frac{(\gamma - 1)\eta \alpha \beta^2}{2\pi(1 + k_p)^{1/2}} \right]^{2/5} \left(\frac{u_1 \zeta}{u_0} \right)^{1/5}. \quad (19)$$

According to Equation (9), $v_h(t) \propto \tilde{L}^{1/2}(t) \sim t^{-2/5}$. Similarly, $v_c(t) \propto P_c^{1/2}(t) \sim t^{-2/5}$. In particular, one can see that $v_h/v_c \sim \theta_0^{-1}$. This means that both the jet head and the cocoon side expand with the same self-similar index $\alpha = \beta = 3/5$ but with different normalization, in agreement with what is described in Appendix B.1.A of Bromberg et al. (2011).

From the latter results we can finally derive the expression for the jet head position as well as for the sideway cocoon extension and recollimation shock height

$$z_h(t) \approx 2 L_j^{1/5} \rho_A^{-1/5} t^{3/5} \theta_0^{-4/5} \left[\frac{\eta(\gamma - 1)(u_0/u_1)^2(1 + k_p)^2}{\pi \zeta^2} \right]^{1/5} \quad (20)$$

$$R_c(t) \approx L_j^{1/5} \rho_A^{-1/5} t^{3/5} \theta_0^{1/5} \left[\frac{\eta(\gamma - 1)}{\pi(1 + k_p)^{1/2}} \right]^{1/5} \left(\frac{u_1 \zeta}{u_0} \right)^{1/10} \quad (21)$$

$$\hat{z}(t) \approx 2 L_j^{3/10} \rho_A^{-3/10} t^{2/5} \theta_0^{-1/5} u_0^{-1/2} \left[\frac{(1 + k_p)(u_0/u_1)}{\zeta \eta^2 \pi^3 (\gamma - 1)^2} \right]^{1/10} \quad (22)$$

We notice that, the jet head and the recollimation shock height share the same self-similar scalings of the astrophysical wind bubble (Weaver et al. 1977; Morlino et al. 2021). We further discuss this aspect in Appendix A.

Finally, following Bromberg et al. (2011), we assume $\eta \approx 1$, which corresponds to a fully adiabatic cocoon valid when radiative losses are negligible. If, on the contrary, energy losses are relevant, the effect of $\eta < 1$ is to move the position of the recollimation shock farther away from the central object and, at the same time, to reduce the distance of the jet head, so that the size of the downstream is reduced. For example, assuming $\eta = 0.01$ the recollimation shock moves farther by a factor ~ 2.5 while the jet head gets closer by the same factor. We discuss the possible impact of this on the maximum energy of accelerated particles in Section 4.5.

3. Particle acceleration model

Jets are extremely complex systems characterized by several plausible processes and locations able to accelerate particles. A non comprehensive list includes DSA at shocks (e.g. forward, reverse, re-collimation and internal), shear acceleration in the jet or at its borders (Rieger 2019), magnetic reconnection (Sironi et al. 2015) and turbulent acceleration (i.e. second-order Fermi process) (see Comisso & Sironi 2018; Matthews et al. 2020; Lemoine 2021, and references therein). In non-relativistic collimated jets, at large distances from the central engine where the flow is likely matter-dominated, DSA represents the primary particle acceleration mechanism. In this respect, jets are somewhat similar to wind bubbles. In this work, we consider an idealized system focusing our attention on a jet at an advanced evolutionary stage that allows us to approximate the acceleration and transport of high-energy particles as steady in time. We focus on the recollimation shock, hereafter labeled with the subscript sh , as the most relevant site for DSA to take place, and we identify its position with \hat{z} as described in Equation (22). We leave, instead, to a follow-up investigation the description of particle acceleration at the reverse and forward shocks at the jet head, given the complexity of particle dynamics in this region, determined by lateral advection and particle escape.

In what follows we develop an analytic modeling of the jet structure in Section 3.1 and we provide a detailed description of our assumptions for the magnetic field and their impact on the diffusion coefficients. In Section 3.2 we describe our acceleration and transport model. In Appendix C we provide analytic results describing different scenarios of turbulence decay in the downstream region.

3.1. General properties of the system

The jet is launched by a central engine with terminal velocity V_w and mass loss rate \dot{M} . As it travels along the launch direction, z , the outflow is also subject to lateral expansion. According to our dynamical model—described in Section 2—the jet expands conically with an opening angle θ_0 up to the recollimation shock where it is focused along the direction of the axis. We parametrize the jet geometry in terms of a height-dependent area

$$A(z) = \begin{cases} \pi z^2 \tan^2 \theta_0 & z \lesssim z_{sh} \\ \pi z_{sh}^2 \tan^2 \theta_0 & z \gtrsim z_{sh} \end{cases} \quad (23)$$

The behavior of the magnetic field in non-relativistic and mildly relativistic jets, especially when far from the central engine, is highly uncertain. We thus assume sub-equipartition between the fluid ram pressure ρu^2 and the magnetic field pressure $B^2/8\pi$, parameterizing with ϵ_B the fraction of ram pressure converted into magnetic energy density. Finally, we assume the latter to be mostly of turbulent nature. We stress that $\epsilon_B \ll 1$ so that the magnetic turbulence does not play a dynamically relevant role. We consider that the magnetic field has a typical coherence length l_c and cascades toward smaller scales with a spectral index δ . At the recollimation shock we consider a magnetic field compression by a factor $\sqrt{11}$.

The parametrization of the magnetic field and the turbulence cascade allows us to characterize the diffusion coefficient as

$$D(z, p) = \frac{v(p)}{3} \begin{cases} r_L(z, p)^{2-\delta} l_c^{\delta-1} & r_L \leq l_c \\ l_c [r_L(z, p)/l_c]^2 & r_L \geq l_c \end{cases} \quad (24)$$

where we account both for the quasi-linear theory, valid for Larmor radii $r_L < l_c$, as well as the small pitch angle scattering

regime taking place for $r_L > l_c$ (see e.g. Subedi et al. 2017; Dundovic et al. 2020). In this work, we assume the jet diameter at the shock as the natural injection scale of the turbulence, i.e. $l_c \simeq 2\hat{z} \tan \theta_0$. We focus on three typical scalings of the turbulence: Bohm ($\delta = 1$), Kraichnan ($\delta = 3/2$) and Kolmogorov ($\delta = 5/3$). The adoption of three different phenomenological diffusion models and their scalings provides insight into the possible outcomes of different diffusion theories, such as mirror diffusion (Lazarian & Xu 2021; Barreto-Mota et al. 2025). Finally, we account for the fact that turbulence may decay along the z axis in the downstream, which, in turn, will reflect in an increasing diffusion coefficient. To this end, we explore different decay laws producing either power-law scaling, $D \propto z$ or $\propto z^2$, or exponential scaling, $D \propto e^{-z/Nl_c}$, where N is the number of coherence lengths after which the turbulence level becomes negligible.

3.2. Acceleration and transport

We consider only the transport along the jet axis direction in a system where the jet section may expand with altitude while we neglect lateral escape. This can be motivated by a suppressed diffusion perpendicular to the jet axis resulting from the typical topology of magnetic-field lines in jets, which are either aligned with the jet axis or wrapped around it. Nevertheless, the impact on the transport of a possible lateral escape as well as an energy loss term is discussed in Appendix B. We thus model the system adopting the one-dimensional stationary transport equation:

$$A(z)u(z) \frac{\partial f(z, p)}{\partial z} = \frac{\partial}{\partial z} \left[A(z)D(z, p) \frac{\partial f(z, p)}{\partial z} \right] + \frac{1}{3} p \frac{\partial f(z, p)}{\partial p} \frac{\partial [A(z)u(z)]}{\partial z} + A(z)Q(z, p) \quad (25)$$

where f is the phase space density of accelerated particles which depends on the spatial coordinate z and momentum p . u is the plasma speed, D the diffusion coefficient and A is the z -dependent function describing the expansion of the wind transverse section. The injection term Q reads as follows:

$$Q(z, p) = Q_{sh}(p) \delta[z - z_{sh}] = \eta_{eff} \frac{n_0 u_{0,n}}{4\pi p^2} \delta[p - p_{inj}] \delta[z - z_{sh}] \quad (26)$$

where n_0 and $u_{0,n}$ are the gas density and wind speed in the immediate upstream of the wind termination shock, while η_{eff} is the fraction of all upstream thermal protons getting injected in the DSA process. Notice that, the upstream wind velocity at the shock u_0 coincides with the terminal wind speed, while the projection along the shock normal is $u_{0,n} = u_0 \sin \psi$. The injection is localized at the termination shock position, z_{sh} , and the injection momentum is $p_{inj} = m_p c$. Notice also that lower injection momenta would not have a relevant impact as their contribution to the pressure at the shock would be subdominant.

In agreement with the cylindrical approximation, the velocity profile is assumed as

$$u(z) = u_0(z) + [u_1(z) - u_0(z)] \theta[z - z_{sh}], \quad (27)$$

where the upstream velocity, u_0 , is connected to the downstream one, u_1 , through the jump conditions typical of strong shocks, namely $u_{0,n} = r u_{1,n}$, where r is the compression ratio. Here we assume the value $r = 4$ of strong shocks. We stress that the jump condition holds for the component along the shock normal, whereas the tangential one is conserved, $u_{0,t} = u_{1,t}$. For the upstream wind we assume a fast rising profile that approaches 0 at $z = 0$. As the wind launching region is much smaller than the

typical diffusion length of particles able to propagate upwind, the details of the wind profile for $z \rightarrow 0$ do not have an impact on our results. Therefore, for simplicity we parametrize the upstream wind adopting a $\tan^{-1}(z)$ profile that quickly converges to the terminal wind speed u_0 . In the downstream region, we assume a constant wind profile $u_1(z) = u_1$. The gas number density at the shock is defined consistently with the jump conditions of the normal component of the wind velocity. The gas profile, the jet area and the wind speed obey the mass conservation equation

$$A(z)\rho(z)u(z) = \dot{M}, \quad (28)$$

where $\rho = nm_p$ is the gas mass density in the jet. Consequently, the knowledge of A and u sets also the gas density profile.

3.2.1. Upstream

To find the general solution of Equation (25) we adopt an iterative technique similar to the one described in Morlino et al. (2021); Peretti et al. (2022, 2023, 2025b); Mukhopadhyay et al. (2023). For $z < z_{\text{sh}}$ we indicate $f(z_{\text{sh}}, p) = f_{\text{sh}}(p)$, while we assume that the system is symmetric with respect to the plane $z = 0$. This leads to a null net flux condition at $z = 0$ which, for realistic wind profiles characterized by no discontinuities, namely $u(0) = 0$, leads to the condition $\partial_z f|_{z=0} = 0$.

We approach the upstream solution by integrating Equation (25) from $z_{\text{min}} = 0$ up to a generic $z < z_{\text{sh}}$. The result is

$$A(z)D_0(z, p)\partial_z f_0(z, p) = A(z)u_0(z)f_0(z, p) + G_0(z, p), \quad (29)$$

where the subscript 0 refers to upstream parameters and

$$G_0(z, p) = \frac{1}{3} \int_0^z dz' f_0(z', p) \partial_{z'} [A(z')u_0(z')] g_0(z', p), \quad (30)$$

$$g_0(z, p) = -\frac{d \ln p^3 f_0(z, p)}{d \ln p}. \quad (31)$$

Physically, Equation (29) states that the balance between the diffusing flux, $-AD\partial_z f$, and the advected flux, Auf , is broken by the function G_0 , which accounts for adiabatic losses/gain, the geometry of the system and its size. In Equation (29) one can recognize a total derivative with respect to the spatial coordinate, so that it can be rewritten as

$$\partial_z \left\{ f_0(z, p) \exp \left[\int_z^{z_{\text{sh}}} dz' \frac{u_{\text{eff},0}(z', p)}{D_0(z', p)} \right] \right\} = 0, \quad (32)$$

where the effective velocity $u_{\text{eff},0}$ is defined as follows:

$$u_{\text{eff},0}(z, p) = u_0(z) \left[1 + \frac{G_0(z, p)}{A(z)u_0(z)f_0(z, p)} \right]. \quad (33)$$

Requiring that the solution is continuous at the recollimation shock, namely $f_0(z_{\text{sh}}, p) = f_{\text{sh}}(p)$, it is straightforward to obtain the general solution to Equation (32):

$$f_0(z, p) = f_{\text{sh}}(p) \exp \left[- \int_z^{z_{\text{sh}}} dz' \frac{u_{\text{eff},0}(z', p)}{D_0(z', p)} \right]. \quad (34)$$

In this upstream solution one can recognize the same behavior of the infinite planar shock solution that gets exponentially suppressed with distance from the shock.

3.2.2. Downstream

For the downstream region, as boundary conditions we require continuity of the particle distribution function at the recollimation shock, namely $f_1(z_{\text{sh}}, p) = f_{\text{sh}}(p)$, while we assume a free escape boundary at the jet head $f(z_{\text{esc}}, p) = 0$.

In analogy with the upstream region, we perform a spatial integration of Equation (25) from $z > z_{\text{sh}}$ up to z_{esc} . The result reads:

$$A(z)D_1(z, p)\partial_z f_1(z, p) - A(z)u_1(z)f_1(z, p) + G_1(z, p) = -A(z_{\text{esc}})j_{\text{esc}}(p), \quad (35)$$

where the subscript 1 refers to the quantity evaluated in the downstream region and $j_{\text{esc}} = -D_1\partial_z f|_{z=z_{\text{esc}}}$ is the escaping flux. The function G_1 appearing in Equation (35) reads

$$G_1(z, p) = \frac{1}{3} \int_z^{z_{\text{esc}}} dz' f_1(z', p) \partial_{z'} [A(z')u_1(z')] g_1(z', p) \quad (36)$$

$$g_1(z, p) = -\frac{d \ln p^3 f_1(z, p)}{d \ln p}. \quad (37)$$

Notice that, qualitatively, Equation (35) has the identical physical interpretation of Equation (29). The main difference here is that, in addition to the adiabatic term, an escape term also appears. Similarly to the upstream region, it is possible to recognize in Equation (35) a total derivative. Performing another spatial integration and adopting the continuity condition at the recollimation shock, one obtains the following:

$$f_1(z, p) \exp \left[- \int_{z_{\text{sh}}}^z dz' u_{\text{eff},1}(z', p) / D_1(z', p) \right] = f_{\text{sh}}(p) - A(z_{\text{esc}})j_{\text{esc}}(p)I(z, p), \quad (38)$$

where

$$I(z, p) = \int_{z_{\text{sh}}}^z dz' \frac{\exp \left[- \int_{z_{\text{sh}}}^{z'} dz'' u_{\text{eff},1}(z'', p) / D_1(z'', p) \right]}{A(z')D_1(z', p)}, \quad (39)$$

$$u_{\text{eff},1}(z, p) = u_1(z) \left[1 - \frac{G_1(z, p)}{A(z)u_1(z)f_1(z, p)} \right]. \quad (40)$$

Applying the free escape boundary condition, $f(z_{\text{esc}}, p) = 0$, to Equation (38) we get the expression of the escaping flux:

$$j_{\text{esc}}(p) = f_{\text{sh}}(p) \frac{1}{A(z_{\text{esc}})I(z_{\text{esc}}, p)}. \quad (41)$$

Finally, the downstream solution can be obtained combining Equation (38) and Equation (41), which gives:

$$f_1(z, p) = f_{\text{sh}}(p) \exp \left[\int_{z_{\text{sh}}}^z dz' \frac{u_{\text{eff},1}(z', p)}{D_1(z', p)} \right] \left[1 - \frac{I(z, p)}{I(z_{\text{esc}}, p)} \right]. \quad (42)$$

Interestingly, as detailed in Appendix C, the downstream solution acquires a simple analytic form for the cases of turbulence decay of our interest, as described in Section 3.1.

3.2.3. Recollimation shock

We assume that the fluid experiences an average angle of impact with the shock surface $\psi_{\text{eff}} = 3\theta_0/4$, obtained mediating Equation (15) between \bar{z} and \hat{z} . These approximations allow us to preserve the 1D description of the acceleration and transport model.

The solution at the termination shock is found integrating the transport equation in an infinitely small spatial range around the termination shock, namely from z_{sh}^- up to z_{sh}^+ . The result of the integration, leads to a projection along the shock normal which reads

$$0 = [\sin \psi^* D \partial_z f] \Big|_{z_{\text{sh}}^-}^{z_{\text{sh}}^+} - \frac{(u_{0,n} - u_{1,n})}{3} p \partial_p f_{\text{sh}}(p) + Q_{\text{sh}}(p), \quad (43)$$

where ψ^* is the angle between the shock surface and the fluid velocity vector. In particular, $\psi^* = \psi_{\text{eff}}$ in the upstream region, while its value in the downstream is found consistently with the compression of the velocity along the shock normal. In the adiabatic term, we used the identity $\partial_z \theta [z - z_{\text{sh}}] = \delta [z - z_{\text{sh}}]$ and the advective term (left hand side) goes to 0 after an integration by parts. Substituting in Equation (43) the expressions of Equations (29) and (35) one obtains the following:

$$\frac{s Q_{\text{sh}}(p)}{u_{0,n} p} = \partial_p f_{\text{sh}}(p) + \frac{s}{p} f_{\text{sh}}(p) + \frac{s}{p} \frac{G_0(z_{\text{sh}}, p)}{A(z_{\text{sh}}) u_0 f_{\text{sh}}(p)} f_{\text{sh}}(p) + \frac{s}{r p} f_{\text{sh}}(p) \left[\frac{G_1(z_{\text{sh}}, p)}{u_1 A(z_{\text{sh}}) f_{\text{sh}}(p)} + \frac{1}{u_1 A(z_{\text{sh}}) \mathcal{I}(z_{\text{esc}})} - 1 \right], \quad (44)$$

where $s = 3u_{0,n}/(u_{0,n} - u_{1,n})$. In the latter expression it is possible to recognize a total derivative so that it can be rewritten as:

$$\partial_p [f_{\text{sh}}(p) p^s e^{\tilde{\Gamma}_0(p)} e^{\tilde{\Gamma}_1(p)}] = \frac{s}{u_{0,n}} \frac{Q_{\text{sh}}(p)}{p} p^s e^{\tilde{\Gamma}_0(p)} e^{\tilde{\Gamma}_1(p)}, \quad (45)$$

where the functions appearing in the exponential are defined as

$$\tilde{\Gamma}_0(p) = s \int_{p_0}^p \frac{dp'}{p'} \frac{G_0(z_{\text{sh}}, p')}{A(z_{\text{sh}}) u_0 f_{\text{sh}}(p')} \quad (46)$$

$$\tilde{\Gamma}_1(p) = \frac{s}{r} \int_{p_0}^p \frac{dp'}{p'} \left[\frac{G_1(z_{\text{sh}}, p')}{u_1 A(z_{\text{sh}}) f_{\text{sh}}(p')} + \frac{1}{u_1 A(z_{\text{sh}}) \mathcal{I}(z_{\text{esc}})} - 1 \right], \quad (47)$$

where p_0 is an arbitrarily low value in the momentum scale smaller than p_{inj} . It is now possible to integrate (45) and obtain the following result for the solution at the termination shock

$$f_{\text{sh}}(p) = \eta_{\text{eff}} \frac{sn_0}{4\pi p_{\text{inj}}^3} \left(\frac{p}{p_{\text{inj}}} \right)^{-s} e^{-\tilde{\Gamma}_0(p)} e^{-\tilde{\Gamma}_1(p)}, \quad (48)$$

where $\Gamma_{0,1}(p) = \tilde{\Gamma}_{0,1}(p) - \tilde{\Gamma}_{0,1}(p_{\text{inj}})$.

The general solution of the transport equation is found with an iterative algorithm that the interested reader can find in Appendix D. Finally, in Appendix E we discuss some analytic aspects of the general solution and possible similarities with the wind termination shock in wind bubbles.

4. Results

Even though they have qualitative similarities in the structure and the dynamics, the power content and the size of jets from protostars, microquasars and active galaxies belong to completely different classes. In light of this, we found practical to set one reference setup as a prototype source for each of the above mentioned classes. In Table 4 we report the relevant parameters assumed with the computed maximum energies for the accelerated particles. For each class, we explored different diffusion coefficients, from the most efficient in scattering, Bohm ($\delta = 1$), to the least efficient, Kolmogorov ($\delta = 5/3$). As its properties lie somewhat in between, we adopt the Kraichnan diffusion coefficient ($\delta = 3/2$) as a benchmark. In addition, for simplicity,

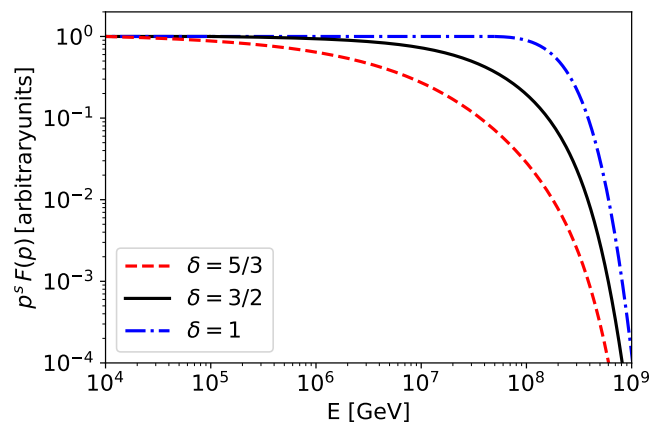


Fig. 3. Seyfert prototype. Spectra of accelerated particles at the recombination shock. The blue dot-dashed curve represents the Bohm scenario, while the solid black and the dashed red represent the Kraichnan and Kolmogorov cases, respectively.

we adopt as a reference, the scenario of spatially constant downstream diffusion coefficient (see Appendix C), while we discuss in Section 4.5 the impact of magnetic turbulence decay in the downstream. Table 4 also reports the main references where such parameter values can be retrieved. In the following, we discuss the different source classes in Sections 4.1–4.3. We delve into the maximum energy with analytic estimates in Section 4.4. In Section 4.5 we evaluate the dependence of particle spectra on the main parameters. We finally comment on the multi-messenger emission from these systems in Section 4.6.

4.1. Prototype Seyfert jet

Seyfert jets are among the weakest and slowest collimated outflows launched by accreting supermassive black holes in active galaxies. They typically feature a large variability in mass loss rate and mildly relativistic wind speed. The prototypical kinetic power of these jets, around $L_{\text{kin}} = 10^{42} \text{ erg s}^{-1}$, is inferred for both NGC 1068 (see Padovani et al. 2024, and references therein) and NGC 4151 (Ulvestad et al. 2005; Williams et al. 2017). To our knowledge, the opening angle of weak radio jets in Seyfert is not well constrained, so we assume $\theta_0 = 10^\circ$ as a benchmark. In the central parsecs of Seyfert galaxies the interstellar medium is significantly denser than the average one. Therefore, we adopt an effective density of $n_A = 10^3 \text{ cm}^{-3}$ (Sánchez-García et al. 2022). We set the typical age of Seyfert jets to $T_{\text{age}} = 10^5 \text{ yr}$, which corresponds to a fraction 1–10% of the typical AGN duty cycle. Finally, we assume a typical value of $\epsilon_B = 10^{-5}$, which allows the recombination shock to remain super-Alfvénic while maintaining magnetic field strengths in the typical range of 0.1–1 mG, as inferred from radio knots observations (Gallimore et al. 1996b; Williams et al. 2017). The reference set of parameters for the prototypical Seyfert jet (SEY₀) are summarized in Table 4.

Figure 3 illustrates the spectra of the solutions at the recombination shock. Bohm diffusion allows to reach the highest energy, $E_{\text{max}} \sim 240 \text{ PeV}$, while Kraichnan and Kolmogorov diffusion allow to reach approximately $\sim 50 \text{ PeV}$ and a few PeV, respectively. One can generally conclude that, depending on the turbulence scenario, Seyfert jets can accelerate particles from PeV up to the EeV range, where the latter can be reached under optimistic parametric assumptions (e.g. small opening an-

Table 1. Prototypical protostellar jets parameters (PS_0) are consistent with HH80-81 as discussed in Rodríguez-Kamenetzky et al. (2017), while those of the prototypical microquasar (MQ_0) are consistent with SS433 as presented in Fabrika (2004). The parameters inferred for the radio jet in NGC 4151 (Ulvestad et al. 2005; Williams et al. 2017) are assumed as prototypical for jets in Seyfert galaxies (SEY_0).

| | \dot{M} [$M_\odot \text{ yr}^{-1}$] | u_0 [km s^{-1}] | θ_0 | n_A [cm^{-3}] | T_{age} [yr] | ϵ_B | $E_{\text{max}} [\delta = 5/3]$ | $E_{\text{max}} [\delta = 3/2]$ | $E_{\text{max}} [\delta = 1]$ |
|---------|---|------------------------------|------------|----------------------------|-----------------------|--------------|---------------------------------|---------------------------------|-------------------------------|
| SEY_0 | 10^{-2} | $3 \cdot 10^4$ | 10° | 10^3 | 10^5 | 10^{-5} | 6 PeV | 50 PeV | 240 PeV |
| MQ_0 | 10^{-6} | $3 \cdot 10^4$ | 2° | 1 | 10^4 | 10^{-5} | 5 PeV | 7 PeV | 8 PeV |
| PS_0 | 10^{-7} | $5 \cdot 10^2$ | 5° | 10^4 | 10^4 | 10^{-5} | 2 GeV | 28 GeV | 4 TeV |

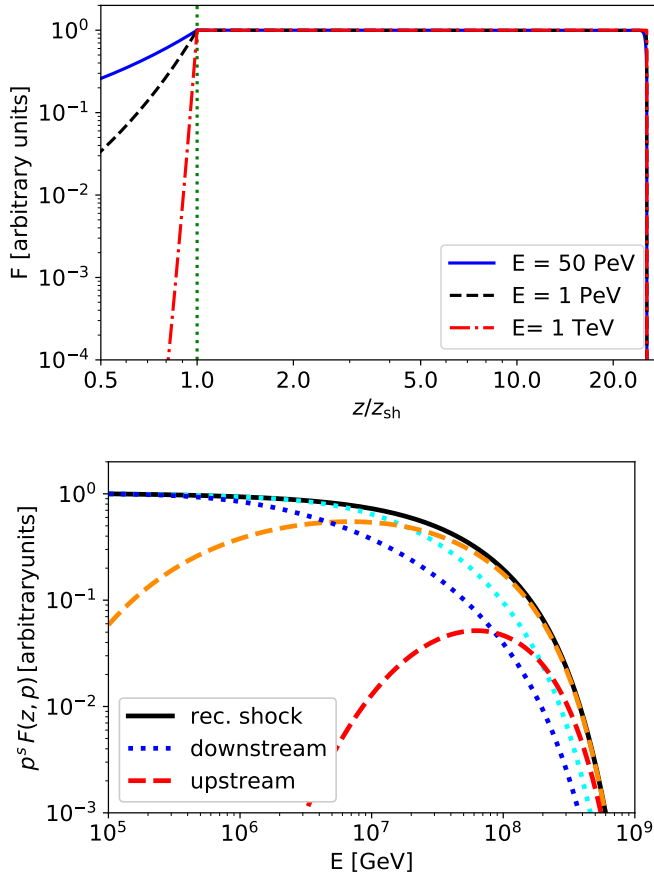


Fig. 4. Radial behavior of the solution for the case of Seyfersts jets. Top panel: particle distribution along z computed at different energies. The vertical dotted line represents the recollimation shock location, while the jet head is located at approximately 20 times z_{sh} . Bottom panel: solution computed at different positions in the jet. The solid black line represents the solution at the shock position while dashed lines refer to the upstream (orange for $z = 0.97 z_{\text{sh}}$ and red for $z = 0.3 z_{\text{sh}}$) and dotted lines to the downstream (cyan and blue for $z \gtrsim 0.98 z_{\text{esc}}$ and $z \gtrsim 0.99 z_{\text{esc}}$ respectively).

gle, high kinetic power and/or Bohm diffusion). It is interesting to notice that, while at low energy all turbulence types predict a power law p^{-s} , the cutoff at higher energies has different shapes, ranging from sharp for the Bohm case to shallower for the Kolmogorov case, with the Kraichnan case falling in between. Such a behavior is analogous to what expected from DSA models in stellar wind bubbles (Morlino et al. 2021; Peretti et al. 2022, 2023, 2025b; Mukhopadhyay et al. 2023).

Figure 4 illustrates how particles behave in the system for the case of prototype Seyfert ($\delta = 3/2$). The top panel illustrates the particle distribution as a function of altitude—in the jet—at different energies. The upstream region exhibits an exponential

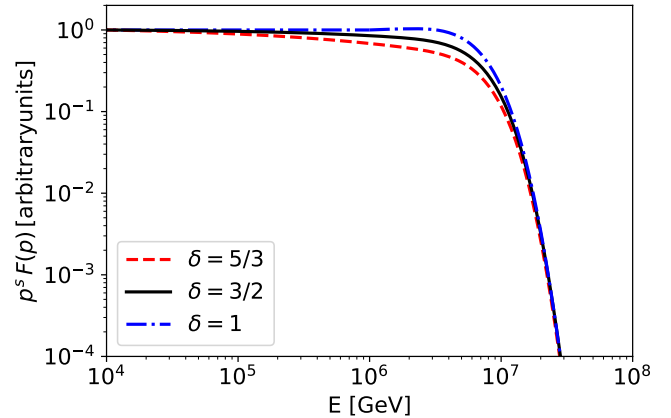


Fig. 5. Microquasar prototype. Particle spectra at the recollimation shock. The linestyle and colors are identical to Figure 3.

decay away from the shock, regulated by the diffusion length D_0/u_0 , as is typical in DSA. In particular, only the highest energy particles can propagate sufficiently far upstream against the jet flow. The downstream region is almost completely dominated by advection. This results in the approximately homogeneous distribution, from the recollimation shock up to the jet head. The bottom panel illustrates the behavior of particle spectra throughout the jet. Dashed lines correspond to locations in the upstream, while dotted lines to locations in the downstream. The upstream spectra clearly show that only the highest energy particles propagate against the jet flow, while the downstream spectra feature the softening due to diffusion while approaching the escape surface at the jet head.

4.2. Prototype microquasar jet

Inspired by the mildly relativistic velocities inferred for SS433 (Marshall et al. 2002), we adopt a conservative jet speed of the order of $0.1c$ and a mass loss rate comparable with the estimated total kinetic power (Fabrika 2004). We assume a typical opening angle of $\theta_0 = 2^\circ$ and an age of 10^4 yrs (Fabrika 2004). Finally, we consider an external medium density comparable with the one of the Galactic interstellar medium, $n_A \approx 1 \text{ cm}^{-3}$, and we assume a value for ϵ_B (10^{-5}) that allows for a magnetic field of the order of a few $10 \mu\text{G}$, compatible with measurements of knots in SS433 (Tsuji et al. 2025), and guaranteeing the shock to be super-Alfvénic. The parameters for the prototypical microquasar (MQ_0) can be found in Table 4.

Differently from the Seyfert case, the maximum energy is approximately falling in the transition region to weak diffusion ($r_L \approx l_c$), where all types of diffusion behave approximately in the same way, resulting in a similar maximum energy. This can be clearly seen in Figure 5, where the spectra resulting from the three diffusion scenarios are compared. As one can also see from

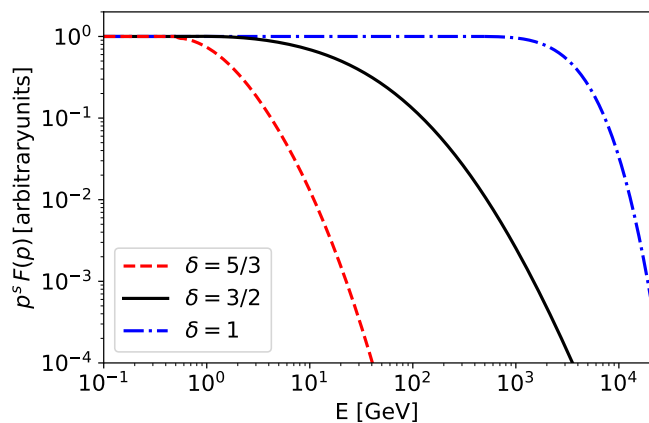


Fig. 6. Protostar prototype. Particle spectra at the recollimation shock. The linestyle and colors are identical to Figure 3.

Table 4, the range of maximum energies varies within less than a factor 2, from ~ 5 to ~ 8 PeV.

4.3. Prototype protostellar jet

Protostellar jets are the slowest class of astrophysical collimated jets. Their typical velocity ranges from about 10^2 km s $^{-1}$ up to 10^3 km s $^{-1}$ and their mass loss rate can exceed 10^{-7} M_{\odot} yr $^{-1}$ (see e.g. Rodríguez-Kamenetzky et al. 2017; Araudo et al. 2021). The jet half-opening angle is expected to range from a few degrees up to ten degrees, and the period of activity can extend for several tens of kilo-years (Frank et al. 2014). As density of the surrounding medium we adopt $n_A = 10^4$ cm $^{-3}$, which is typical of giant molecular clouds, where protostellar system are likely to be found. Finally, we assume $\epsilon_B = 10^{-5}$, which guarantees that the shock is super-Alfvénic with a magnetic field strength of $B \approx 40 \mu\text{G}$. Such value agrees with the magnetic field expected at a distance of 0.1 pc from the protostar if the field at its surface is of the order of mG to G. The parameters for the prototypical protostellar jet (PS $_0$) are summarized in Table 4.

As done for the previous source classes, in Figure 6 we show the spectra of accelerated particles at the recollimation shock. It is possible to see that the maximum energy changes significantly between different diffusion scenarios. In particular, Kolmogorov diffusion seems unable to efficiently energize protons above a couple of GeV, while Kraichnan and Bohm diffusion allow to reach a few tens of GeV and a few TeV, respectively. The computed values of the maximum energies for the different diffusion scenarios are reported in the last columns of Table 4. We notice also that, given the typical size of the system of $\sim 0.1 - 1$ pc, energy losses due to Coulomb scattering and ionization as well as pp interactions at high energy do not play a relevant role on the scales of our interest, namely at the location of the recollimation shock.

4.4. Qualitative considerations on the maximum energy

The maximum energy of particles accelerated at the recollimation shock of jets is one of the main results of this work. Despite the fact that there are several parameters that influence the maximum energy, it is very useful to discuss qualitative estimates that are naturally set by the size of the system. In particular, the upstream region, compared to the downstream one, can be expected to set the most stringent conditions unless the turbulence decays

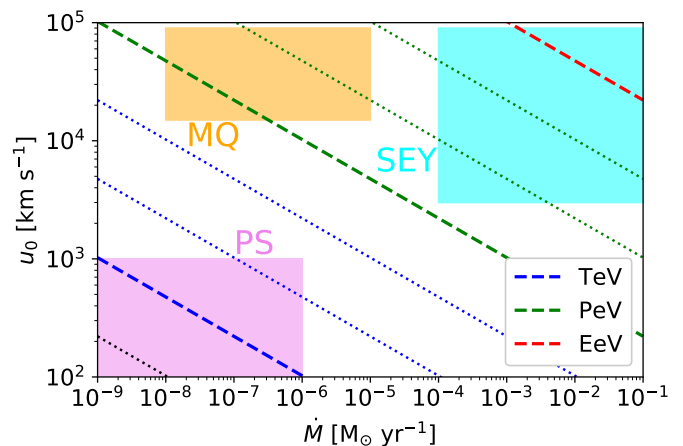


Fig. 7. Mass-loss rate to terminal wind speed ($\dot{M} - u_0$) parametric plot of the maximum energy achievable by the sub-relativistic jet classes analyzed in this work assuming the typical opening angle of 4° for all three source classes. PS, MQ and SEY stand respectively for protostar (pink), microquasar (orange) and Seyfert (cyan). The diagonal lines indicate the different decades in maximum energy. The energy increases from bottom left (10^2 GeV) to top right (EeV). The dashed lines represent respectively TeV, PeV and EeV, while the dotted ones are intermediate decades.

extremely rapidly after the recollimation shock (see Section 4.5 for a detailed discussion).

An estimate of the maximum energy can be obtained assuming that the upstream diffusion length of particles at the maximum energy, $D(E_{\text{max}})/u_0$, is as large as the upstream region itself, z_{sh} . Here u_0 identifies the upstream velocity. The latter condition is the analog of the Hillas criterion (Hillas 1984), and in order to obtain an upper limit, we also assume Bohm diffusion. Recalling that the magnetic field pressure can be parametrized as a fraction ϵ_B of the ram pressure, we obtain the following general analytic expression

$$E_{\text{max}} \lesssim 3 \left(\frac{\epsilon_B}{10^{-5}} \right)^{1/2} \left(\frac{\dot{M}}{10^{-6} M_{\odot} \text{ yr}^{-1}} \right)^{1/2} \left(\frac{u_0}{0.1 c} \right)^{3/2} \left(\frac{\theta_0}{4^\circ} \right)^{-1} \text{ PeV} \quad (49)$$

It is interesting to notice that the dependence of E_{max} on the mass-loss rate \dot{M} and on the velocity u_0 is identical to the wind bubble scenario (Peretti et al. 2025b), whereas in the case of jets, there is an additional dependence on the inverse of the jet opening angle. The latter dependence is crucial for allowing jets to reach extremely high energies while the magnetic field can be dynamically subdominant.

We observe that, in general, the combination of Bohm diffusion and the equality between the diffusion length and the size of the upstream should set an upper limit to the maximum energy. However, we point out that this is not necessarily the case in the context of our model. In fact, high energy particles that are propagating sufficiently far in the upstream region experience a higher magnetic field and, in turn, a smaller diffusion coefficient—this is a natural result of our parametrization of the magnetic field, $P_B = \epsilon_B P_{\text{ram}}$. Such a space-dependence of the magnetic field can result in maximum energies slightly exceeding the estimate provided in Equation (49), without resulting in a violation of the Hillas criterion.

Figure 7 compares the maximum energy of the three jet classes analyzed in this work as a function of \dot{M} and u_0 adopting the same opening angle $\theta_0 = 4^\circ$. It is possible to observe

Table 2. Parameter space scan. Impact on the maximum energy of different parametric assumptions. In the first row, for reference we report the maximum energy for the three prototypes presented in Table 4. The first column reports the parameter modified with respect to the prototype. The three columns in the table refer respectively to protostar (PS), microquasar (MQ) and Seyfert (SEY). Missing entries in the Table are meant to emphasize lack of differences with respect to the prototype.

| | E_{\max} (PS) | E_{\max} (MQ) | E_{\max} (SEY) |
|--------------------------------|-----------------|-----------------|------------------|
| prototype | 28 GeV | 7 PeV | 50 PeV |
| $2 u_0$ | 150 GeV | 18 PeV | 278 PeV |
| $1/2 u_0$ | 8 GeV | 2 PeV | 9 PeV |
| $10 \dot{M}$ | 80 GeV | 22 PeV | 162 PeV |
| $10^{-1} \dot{M}$ | 11 GeV | 2 PeV | 16 PeV |
| $10 \epsilon_B$ | 80 GeV | 22 PeV | 162 PeV |
| $10^{-1} \epsilon_B$ | 11 GeV | 2 PeV | 16 PeV |
| $10 n_A$ | - | - | - |
| $10^{-1} n_A$ | - | - | - |
| $10 T_{\text{age}}$ | - | - | - |
| $10^{-1} T_{\text{age}}$ | - | - | - |
| $2 \theta_0$ | 9 GeV | 3 PeV | 11 PeV |
| $1/2 \theta_0$ | 100 GeV | 13 PeV | 200 PeV |
| $10^{-1} l_c$ | 266 GeV | 4 PeV | 130 PeV |
| $\eta = 0.01$ | - | - | - |
| $\Delta_{\text{down}} = l_c$ | 10 GeV | 1 PeV | 32 PeV |
| $\Delta_{\text{down}} = 3 l_c$ | 23 GeV | 4 PeV | 47 PeV |
| $\alpha = 1$ | - | - | - |
| $\alpha = 2$ | - | - | 47 PeV |

that protostellar jets are limited to the GeV-TeV energy domain; Microquasars can be expected to accelerate particles from hundreds of TeV up to tens of PeV for the most extreme sources, while Seyfert jets can accelerate particles from PeV up to the EeV domain.

We finally point out that, while the scaling with \dot{M} can be expected for all the considered diffusion scenarios, the scaling $E_{\max} \sim u_0^{3/2}$ is a result limited to Bohm diffusion. For a generic turbulence slope of index δ one can expect the dependence on the velocity to become of the order $E_{\max} \sim u_0^{(4-\delta)/(4-2\delta)}$ with some possible fluctuations due to the dependence of E_{\max} also on $z_{\text{sh}}^{(\delta-1)/(2-\delta)}$, where z_{sh} , in turn, mildly depends on u_0 with a power law index 0.1. We additionally observe a possible dependence of the maximum energy on the coherence length of the magnetic field as $E_{\max} \sim l_c^{(1-\delta)/(2-\delta)}$. In practice, we adopt a physically motivated reference value for l_c and, in the absence of additional relevant scales in the problem, we do not treat it as a free parameter. Nevertheless, in the following section we explore the possibility of having a somewhat smaller coherence length.

4.5. Parameter space scan

Although selecting a prototype source offers a qualitative view of the range of maximum particle energies, variability within each jet class can span orders of magnitude—or at least significant factors—for the parameters considered. A complete exploration of the parameter space is beyond the scope of this work; instead, in this subsection we assess the impact of different parameter choices by varying each parameter individually relative to the SEY₀, MQ₀, and PS₀ prototypes, assuming Kraichnan diffusion.

In Table 2 we report the results for E_{\max} obtained by changing the parameters' values by some factor with respect to the benchmark cases. We first vary the velocity by a factor of 2 and

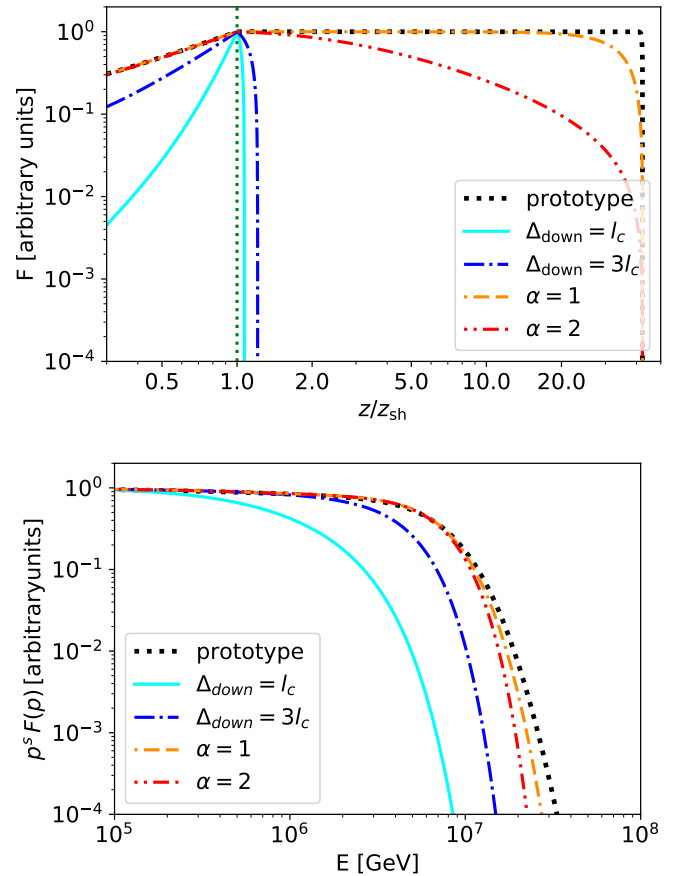


Fig. 8. Impact of different downstream transport conditions for the case of MQ. Top panel: particle distribution along the jet. The green vertical dotted line identifies the recollimation shock location. Bottom panel: spectrum of accelerated particles. The color code and line styles are identical for both plots. The cyan solid line and the blue dot-dashed represent respectively the exponential decay of the turbulence on typical scales l_c and $3 l_c$ respectively. The orange dash-dash-dotted line and red double-dot-dashed line represent respectively the power-law scaling diffusion coefficient with index 1 and 2. The black dotted line is the prototype MQ₀.

the mass loss rate by a factor 10. In all scenarios we observe that the higher the kinetic power the higher the maximum energy. We approximately find that E_{\max} scales with $\dot{M}^{1/2}$ in line with what we discussed in the previous subsection, whereas the scaling with velocity is not the same. In particular, for PS and SEY we observe a dependence *à la Kraichnan*, i.e. $\propto u_0^{2.5}$, while for the MQ the scaling is $\propto u_0^{1.5}$. Such a different scaling derives from the maximum energy being in the transition region where $r_L \approx l_c$. Modifications of ϵ_B have identical scaling as the mass-loss rate. This is due to the assumption that the magnetic pressure is proportional to the ram pressure, which depends linearly on \dot{M} . Modifications of the density and age of the system do not affect E_{\max} because the maximum energy does not depend significantly on the position of the recollimation shock, as Equation (49) shows for the case of Bohm diffusion. Also, this is a consequence of the assumption that $B^2 \propto \rho_0 u_0^2$ and on the additional assumption that l_c is of the same order of the jet diameter.

Similarly to the case of the velocity, we observed that for different assumptions in θ_0 we obtain a Bohm-like scaling for MQ, while SEY and PS feature a stronger dependence resulting from the Kraichnan-like scaling. We also explored the possibility of

having a smaller coherence length by assuming it an order of magnitude smaller than the jet diameter. We observed that in the case of protostar and Seyfert this leads to an increase of E_{\max} , whereas in the case of microquasar the same operation results only in a small decrease. The former case is somewhat trivial, in that smaller l_c results in smaller diffusion coefficient and consequently higher maximum energy. In the latter case, the decrease in the diffusion coefficient normalization is compensated by the transition to the small pitch angle scattering occurring at lower energies.

Changing η to values < 1 increases the distance of the recollimation shock (but this does not affect E_{\max} as already discussed above) and decreases the height of the jet head, thereby reducing the size of the downstream. The latter effect may reduce the maximum energy only if the effective downstream size becomes significantly smaller than the one upstream, as discussed in the following.

We explored different assumptions on the downstream turbulence. We consider two possible scenarios, each of them with two different scalings. The first one assumes that the turbulence decays exponentially throughout the downstream on a typical length-scale comparable to l_c . We implement it by moving the escaping boundary from the jet head to a distance, $\Delta_{\text{down}} = l_c$ and $3 l_c$ from the shock surface. The second scenario assumes a power-law decay of the turbulence in the downstream region resulting in a diffusion coefficient $D \sim z^\alpha$ and we explore it by considering a linear and quadratic scalings, i.e. $\alpha = 1$ and 2 . In Figure 8 we report the spatial distribution of particles (top panel) and the spectra at the recollimation shock (bottom panel) associated to the different transport scenarios considered for the downstream region. For the cases of exponentially decaying turbulence we observe a sizable decrease of the maximum energy, indicating that propagation in the downstream becomes the dominant effect in determining the maximum energy of the system. For the case of power-law decay we observe only a marginal difference in the shape of the cutoff, but the effective maximum energy remains substantially unchanged, meaning that the propagation upstream provides the most stringent constraint. In the case of $D_1 \propto z^2$ we observe a mild decrease of E_{\max} only in the case of Seyfert jets suggesting that, depending on the jet class, the conditions of confinement might become comparable between upstream and downstream.

4.6. Comments on the particle escape from the system and hadronic gamma-ray production regions

The particle transport is in general dominated by the advection with a subdominant impact of diffusion. For all jet classes of our interest, energy losses due to proton-proton collisions are negligible within the jet. Therefore, one can expect that the majority of accelerated protons will either escape the system by crossing the jet head and the forward shock or be advected sideways in the cocoon after crossing the reverse shock and, possibly, the jet lateral surface.

The ultimate fate of high-energy particles in the context of our model depends on the physical and micro-physical conditions they encounter near the outer boundary of the jet, namely at the jet head. A detailed characterization of the jet-head structure, its microphysics, and the lateral advective flows feeding the cocoon goes beyond the scope of this work. However, they can naturally be expected to play a central role—together with a possible lateral escape from the jet—in the way relativistic particles populate the cocoon.

The external cocoon, in turn, is expected to contain enough material to provide an effective target for pp interactions. However, the possibility for such a cocoon to shine in gamma rays highly depends on the local diffusion coefficient (see also Abaroa et al. 2026, for similar discussion in the context of microquasar remnants) and the possible presence of large scale flows connected to the cocoon intrinsic dynamics, an accretion disc wind or the central engine itself.

All these aspects connected to the multi-wavelength and high-energy neutrino emission will be explored in a forthcoming publication. However, it is reasonable to expect that the morphology of hadronic (pp) emission from a jet-cocoon system shall appear as a wide region extending along the whole cocoon size. A somewhat more exotic hadronic channel may come from $p\gamma$ interactions in the vicinity of the central engine. In fact, a non-negligible amount of protons in the cocoon, could be either advected in the backflows or diffuse near the jet launching region where photon fields are strong enough to provide a sizable target. $p\gamma$ interactions might also take place efficiently if the size of the system is extremely compressed, possibly due to a combination of young age and high density of the external medium. On the other hand, depending on the local magnetic field encountered, the leptonic emission, may appear mainly in bright knots and/or localized along the jet spine similarly to what is observed in the case of S433 (H. E. S. S. Collaboration et al. 2024; Tsuji et al. 2025).

5. Discussion and future prospects

The treatment of particle acceleration and transport performed in this work aims at describing the leading-order physics of diffusive shock acceleration at recollimation shocks within a tractable semi-analytical framework. This choice, while allowing for a systematic exploration of parameter space, naturally entails a number of simplifications that we discuss below.

First, the transport equation is solved in a 1D geometry along the jet axis. This approximation neglects transverse gradients and dimensional effects, including lateral particle escape. In realistic jets, especially in non-magnetically dominated flows, perpendicular transport and shear-induced effects may contribute to shaping both the particle spectrum, maximum energy and the spatial distribution of non-thermal emission. Therefore, including multi-dimensional transport and anisotropic diffusion coefficients will be an important step forward. The lateral escape, in particular, might play a substantial role if the Larmor radius approaches the jet diameter—assumed also to be equal to the coherence length. In this context, the existence of regular magnetic field—especially a toroidal component—could strongly limit this effect. We believe that this aspect can motivate further investigations and dedicated simulations.

Second, the present model does not explicitly include a dynamically relevant ordered guiding magnetic field, nor does it account for a strong toroidal component. While this is consistent with the assumption of a kinetically dominated jet at the scales of interest, different magnetic configurations could alter, as said, both the confinement properties and the acceleration efficiency. Extending the framework to include prescribed magnetic geometries and anisotropic diffusion represents a natural improvement.

Related to this point, the obliquity of the recollimation shock is treated only approximately by finding an effective angle of impact between the fluid and the shock. The complexity of particle acceleration at oblique shocks, and its potential implications on the spectral slope and acceleration efficiency when also guide magnetic field are included (Kirk & Heavens 1989; Gieseler

et al. 1999; Bell et al. 2011; Kirk et al. 2023; Shirin T et al. 2025) cannot be fully captured within the current formulation. In particular, the interplay between magnetic field orientation, shock geometry, and particle scattering may introduce potential deviation from the canonical spectral indices discussed here. A more self-consistent treatment of shock obliquity, its extension and magnetic field topology, possibly informed by kinetic or hybrid simulations, will be the focus of future investigations.

The model focuses on acceleration at the recollimation shock, while strong shocks may also be present at the jet head, where both reverse and forward shocks can contribute to non-thermal particle production, or possibly lead to a re-acceleration scenario. Although this does not invalidate the present scenario, a global treatment coupling recollimation and jet head would provide a more comprehensive picture of particle energization in collimated outflows. This aspect will be the focus of a follow-up work in preparation.

Overall, these limitations do not affect the internal consistency of the model, but rather delineate a well-defined domain of applicability and highlight clear directions for systematic extensions, including multi-dimensional transport in different magnetic configurations, oblique shock physics, and relativistic generalizations.

The main limitation of the hydrodynamical description is the assumption of stationarity. Both the jet central engine and the external medium are treated as steady, and the ambient density is assumed to be uniform. While this represents a reasonable first-order approximation and can often be mapped onto effective time-averaged quantities, it cannot capture the intrinsic variability that could characterize some AGN, microquasars, and protostellar systems. Time-dependent activity of the central engine, intermittency, and stratified or magnetized external media (e.g. wind-like density profiles) may significantly affect the location and strength of recollimation shocks as well as producing interesting 3D effects such as kink and sausage instability where other internal shocks could develop. A time-dependent MHD extension of the present framework in complex media would therefore be highly valuable.

The model is developed in the sub-relativistic regime, as an extension of the Bromberg (2011) formalism. As a consequence, it can be safely applied only up to mildly relativistic velocities. This is particularly relevant for AGN jets and microquasars. Many objects in these source classes can reach, in fact, relativistic bulk speeds. A fully relativistic generalization would allow the framework to address more powerful systems, including relativistic microquasars, Fanaroff–Riley (FR) AGN jets and blazars, which are characterized by high kinetic luminosities and relativistic launching speeds. Interestingly, observations indicate that FR jets, while initially relativistic, often show strong deceleration at kiloparsec scales (Kataoka et al. 2008; Mullin & Hardcastle 2009; Reddy et al. 2023), precisely where strong recollimation shocks are expected to develop (Laing & Bridle 2002). Hydrodynamical simulations (e.g. Perucho & Martí 2007; Perucho et al. 2014) suggest that such shocks can be dynamically important and, in some cases, even disrupt the flow (see also Perucho et al. 2019, 2022). Extending the present semi-analytical approach to this relativistic regime represents a promising avenue for future work.

Additional source-dependent limitations should also be noted. In protostellar jets, high densities may imply that the condition $\tilde{L} \ll 1$ is not always satisfied, even at large distances from the source, potentially modifying the recollimation properties. Moreover, magnetic fields may play a non-negligible role

in the collimation process itself (Ustamujic et al. 2016), requiring a magneto-hydrodynamical treatment.

In microquasars associated to high-mass X-ray binaries, the interplay between jet and stellar wind can further complicate the dynamics. If the wind luminosity exceeds the cocoon pressure, the global shock structure and the formation of recollimation shocks may differ from the simplified scenario considered here, such as in the case of Cygnus X-3, one of the most powerful Galactic PeV accelerators (The LHAASO Collaboration et al. 2025), where the massive companion is a Wolf-Rayet star (Koljonen & Maccarone 2017).

Finally, it is worth noting that geometrical configurations similar to those discussed in this work, are not exclusive of recollimation shocks, but can generically occur in internal shocks in jets.

6. Conclusions

In this work, we investigated particle acceleration via diffusive shock acceleration at recollimation shocks in sub-relativistic jets. In order to do so, we formulated a sub-relativistic extension of the hydrodynamics model of the jet-cocoon system as developed by Bromberg et al. (2011). In such a framework, we studied acceleration and transport by solving the space-dependent transport equation in the jet assuming global stationarity and free escape at the jet head and zero net flux at the launching point of the jet. Our model is versatile and was applied to different source classes: Seyfert jets, microquasars, and protostellar jets.

We explored these different jet classes by setting a prototype for each of these objects, and we investigated the impact of different assumptions for particle diffusion. We focused our attention on the spectral shapes and maximum energy of the accelerated particles. We found simple analytic expressions for upper limits to such a maximum energy in each source class finding that Seyfert can accelerate from PeV up to EeV, microquasars up to tens of PeV and protostellar jets up to the TeV range.

We explored the parameter space for each source class finding results in good agreement with our analytic estimates. In general, we found that the upstream region of the recollimation shock poses the most stringent conditions on the maximum available energies. In this context, we explored also the impact of spatially decaying turbulence in the downstream region of the recollimation shock concluding that in certain configurations, the limits imposed by the downstream region might become the dominant ones.

We conclude with an observational perspective. Recollimation shocks and, more generally, internal shocks in collimated jets, might appear as bright knots and shine because of leptonic emission. In this work, we clearly showed that proton inelastic collisions are not expected to be relevant in sub-relativistic collimated jets. However, protons might leak from the jet through either the jet head or laterally and diffuse in the denser cocoon. Depending on the local environmental conditions encountered in cocoons, inelastic proton-proton, and/or possibly $p\gamma$, collisions might result in extended morphologies of hadronic nature.

Acknowledgements. EP acknowledges economic support from INAF through “Assegni di ricerca per progetti di ricerca relativi a CTA e precursori”. Part of this work was carried out at the APC Laboratory, whose hospitality EP gratefully acknowledges. EP is grateful to M. Pais, A. Zegarelli, S. Celli and M. Lemoine for insightful discussions on jet physics. GM and EA are partially supported by the INAF Theory Grant 2024 *Star Clusters As Cosmic Ray Factories II*. SSC acknowledges support from the ANR grant “MiCRO” with the reference number ANR-23-CE31-0016.

References

- Abaroa, L., Romero, G. E., & Bosch-Ramon, V. 2026, *A&A*, 705, L4
- Abaroa, L., Romero, G. E., Mancuso, G. C., & Rizzo, F. N. 2024, *A&A*, 691, A93
- Abeysekera, A. U., Albert, A., Alfaro, R., et al. 2018, *Nature*, 562, 82
- Acharyya, A., Aharonian, F., Ashkar, H., et al. 2025, arXiv e-prints, arXiv:2511.10537
- Araudo, A. T., Padovani, M., & Marcowith, A. 2021, *MNRAS*, 504, 2405
- Araudo, A. T., Romero, G. E., Bosch-Ramon, V., & Paredes, J. M. 2007, *A&A*, 476, 1289
- Atoyan, A. M. & Aharonian, F. A. 1999, *MNRAS*, 302, 253
- Band, D. L. & Grindlay, J. E. 1986, *ApJ*, 311, 595
- Barkov, M. V. & Khangulyan, D. V. 2012, *MNRAS*, 421, 1351
- Barreto-Mota, L., de Gouveia Dal Pino, E. M., Xu, S., & Lazarian, A. 2025, *ApJ*, 988, 269
- Begelman, M. C. & Cioffi, D. F. 1989, *ApJ*, 345, L21
- Bell, A. R., Schure, K. M., & Reville, B. 2011, *MNRAS*, 418, 1208
- Blandford, R. D. & Königl, A. 1979, *ApJ*, 232, 34
- Blandford, R. D. & Payne, D. G. 1982, *MNRAS*, 199, 883
- Blandford, R. D. & Rees, M. J. 1974, *MNRAS*, 169, 395
- Blandford, R. D. & Rees, M. J. 1978, *Phys. Scr.*, 17, 265
- Blandford, R. D. & Znajek, R. L. 1977, *MNRAS*, 179, 433
- Blondin, J. M., Konigl, A., & Fryxell, B. A. 1989, *ApJ*, 337, L37
- Bodo, G. & Tavecchio, F. 2018, *A&A*, 609, A122
- Bordas, P., Bosch-Ramon, V., Paredes, J. M., & Perucho, M. 2009, *A&A*, 497, 325
- Bosch-Ramon, V. 2015, *A&A*, 575, A109
- Bosch-Ramon, V. & Paredes, J. M. 2004a, *A&A*, 417, 1075
- Bosch-Ramon, V. & Paredes, J. M. 2004b, *A&A*, 425, 1069
- Bosch-Ramon, V., Perucho, M., & Bordas, P. 2011, *A&A*, 528, A89
- Bosch-Ramon, V., Romero, G. E., Araudo, A. T., & Paredes, J. M. 2010, *A&A*, 511, A8
- Bosch-Ramon, V., Romero, G. E., & Paredes, J. M. 2005, *A&A*, 429, 267
- Bromberg, O., Nakar, E., Piran, T., & Sari, R. 2011, *ApJ*, 740, 100
- Bykov, A. M., Osipov, S. M., Romansky, V. I., et al. 2025, *Phys. Rev. D*, 112, 063017
- Carrasco-González, C., Sanna, A., Rodríguez-Kamenetzky, A., et al. 2021, *ApJ*, 914, L1
- Cerutti, B., Dubus, G., Malzac, J., et al. 2011, *A&A*, 529, A120
- Churazov, E. M., Khabibullin, I. I., & Bykov, A. M. 2024, *A&A*, 688, A4
- Comisso, L. & Sironi, L. 2018, *Phys. Rev. Lett.*, 121, 255101
- Daly, R. A. & Marscher, A. P. 1988, *ApJ*, 334, 539
- de Oña Wilhelmi, E., López-Coto, R., & Su, Y. 2023, *MNRAS*, 523, 105
- Doi, A., Hada, K., Kino, M., Wajima, K., & Nakahara, S. 2018, *ApJ*, 857, L6
- Dubus, G., Cerutti, B., & Henri, G. 2010, *MNRAS*, 404, L55
- Dundovic, A., Pezzi, O., Blasi, P., Evoli, C., & Matthaeus, W. H. 2020, *Phys. Rev. D*, 102, 103016
- Ehler, D., Oikonomou, F., & Peretti, E. 2025, *MNRAS*, 539, 2435
- Escobar, G. J., Pellizza, L. J., & Romero, G. E. 2021, *A&A*, 650, A136
- Escobar, G. J., Pellizza, L. J., & Romero, G. E. 2022, *A&A*, 665, A145
- Fabrika, S. 2004, *Astrophys. Space Phys. Res.*, 12, 1
- Fermi LAT Collaboration, Abdo, A. A., Ackermann, M., et al. 2009, *Science*, 326, 1512
- Frank, A., Ray, T. P., Cabrit, S., et al. 2014, in *Protostars and Planets VI*, ed. H. Beuther, R. S. Klessen, C. P. Dullemond, & T. Henning, 451–474
- Gallimore, J. F., Baum, S. A., & O’Dea, C. P. 1996a, *ApJ*, 464, 198
- Gallimore, J. F., Baum, S. A., O’Dea, C. P., & Pedlar, A. 1996b, *ApJ*, 458, 136
- Giannios, D. & Spruit, H. C. 2006, *A&A*, 450, 887
- Gieseler, U. D. J., Kirk, J. G., Gallant, Y. A., & Achterberg, A. 1999, *A&A*, 345, 298
- Gómez, J.-L. & Marscher, A. P. 2000, *ApJ*, 530, 245
- Gómez, J. L., Martí, J. M., Marscher, A. P., Ibáñez, J. M., & Alberdi, A. 1997, *ApJ*, 482, L33
- Gomez, J. L., Martí, J. M. A., Marscher, A. P., Ibanez, J. M. A., & Marcaide, J. M. 1995, *ApJ*, 449, L19
- Goodall, P. T., Alouani-Bibi, F., & Blundell, K. M. 2011, *MNRAS*, 414, 2838
- H. E. S. S. Collaboration, Aharonian, F., Ait Benkhali, F., et al. 2024, *Science*, 383, 402
- Hada, K., Doi, A., Wajima, K., et al. 2018, *ApJ*, 860, 141
- Haro, G. 1952, *ApJ*, 115, 572
- Heinz, S. & Sunyaev, R. 2002, *A&A*, 390, 751
- Herbig, G. H. 1951, *ApJ*, 113, 697
- Hillas, A. M. 1984, *ARA&A*, 22, 425
- Kaci, S., Giacinti, G., Aharonian, F., & Wang, J.-S. 2025, arXiv e-prints, arXiv:2510.01369
- Kaiser, C. R. & Alexander, P. 1997, *MNRAS*, 286, 215
- Kantzas, D., Markoff, S., Beuchert, T., et al. 2021, *MNRAS*, 500, 2112
- Kataoka, J., Stawarz, L., Harris, D. E., et al. 2008, *ApJ*, 685, 839
- Khangulyan, D., Bosch-Ramon, V., & Hadasch, D. 2024, *Journal of High Energy Astrophysics*, 43, 93
- Kharb, P., Hota, A., Croston, J. H., et al. 2010, *ApJ*, 723, 580
- Kimura, S. S., Murase, K., & Mészáros, P. 2020, *ApJ*, 904, 188
- Kirk, J. G. & Heavens, A. F. 1989, *MNRAS*, 239, 995
- Kirk, J. G., Reville, B., & Huang, Z.-Q. 2023, *MNRAS*, 519, 1022
- Koljonen, K. I. I. & Maccarone, T. J. 2017, *MNRAS*, 472, 2181
- Komissarov, S. S. & Falle, S. A. E. G. 1997, *MNRAS*, 288, 833
- Konigl, A. & Pudritz, R. E. 2000, in *Protostars and Planets IV*, ed. V. Mannings, A. P. Boss, & S. S. Russell, 759
- Krause, M. 2003, *A&A*, 398, 113
- Laing, R. A. & Bridle, A. H. 2002, *MNRAS*, 336, 328
- Lazarian, A. & Xu, S. 2021, *ApJ*, 923, 53
- Le Nagat Neher, B., Peretti, E., Cristofari, P., & Zech, A. 2026, arXiv e-prints, arXiv:2603.08701
- Lemoine, M. 2021, *Phys. Rev. D*, 104, 063020
- Lenain, J.-P., Ricci, C., Türler, M., Dorner, D., & Walter, R. 2010, *A&A*, 524, A72
- Lhaaso Collaboration, Cao, Z., Aharonian, F., et al. 2025, *National Science Review*, 12, nwaf496
- Markoff, S., Nowak, M. A., & Wilms, J. 2005, *ApJ*, 635, 1203
- Marscher, A. P. & Gear, W. K. 1985, *ApJ*, 298, 114
- Marshall, H. L., Canizares, C. R., & Schulz, N. S. 2002, *ApJ*, 564, 941
- Matthews, J. H., Bell, A. R., & Blundell, K. M. 2020, *New A Rev.*, 89, 101543
- Matthews, J. H., Bell, A. R., Blundell, K. M., & Araudo, A. T. 2019, *MNRAS*, 482, 4303
- Micono, M., Zurlo, N., Massaglia, S., Ferrari, A., & Melrose, D. B. 1999, *A&A*, 349, 323
- Middleton, M. J., Walton, D. J., Alston, W., et al. 2021, *MNRAS*, 506, 1045
- Mirabel, I. F. & Rodríguez, L. F. 1994, *Nature*, 371, 46
- Mirabel, I. F. & Rodríguez, L. F. 1998, *Nature*, 392, 673
- Mizuno, Y., Gómez, J. L., Nishikawa, K.-I., et al. 2015, *ApJ*, 809, 38
- Moll, R., Spruit, H. C., & Obergaulinger, M. 2008, *A&A*, 492, 621
- Monceau-Baroux, R., Porth, O., Meliani, Z., & Keppens, R. 2014, *A&A*, 561, A30
- Morlino, G., Blasi, P., Peretti, E., & Cristofari, P. 2021, *MNRAS*, 504, 6096
- Mukhopadhyay, P., Peretti, E., Globus, N., Simeon, P., & Blandford, R. 2023, *ApJ*, 953, 49
- Mullin, L. M. & Hardcastle, M. J. 2009, *MNRAS*, 398, 1989
- Norman, M. L., Winkler, K. H. A., Smarr, L., & Smith, M. D. 1982, *A&A*, 113, 285
- Ohmura, T., Machida, M., Nakamura, K., Kudoh, Y., & Matsumoto, R. 2020, *MNRAS*, 493, 5761
- Ohmura, T., Ono, K., Sakemi, H., et al. 2021, *ApJ*, 910, 149
- Ouyed, R. & Pudritz, R. E. 1999, *MNRAS*, 309, 233
- Padovani, M., Hennebelle, P., Marcowith, A., & Ferrière, K. 2015, *A&A*, 582, L13
- Padovani, P., Resconi, E., Ajello, M., et al. 2024, *Nature Astronomy*, 8, 1077
- Penrose, R. 1969, *Nuovo Cimento Rivista Serie*, 1, 252
- Peretti, E., Lamastra, A., Saturni, F. G., et al. 2023, *MNRAS*, 526, 181
- Peretti, E., Morlino, G., Blasi, P., & Cristofari, P. 2022, *MNRAS*, 511, 1336
- Peretti, E., Peron, G., Tombesi, F., et al. 2025a, *J. Cosmology Astropart. Phys.*, 2025, 013
- Peretti, E., Petropoulou, M., Vasilopoulos, G., & Gabici, S. 2025b, *A&A*, 698, A188
- Perucho, M. & Martí, J. M. 2007, *MNRAS*, 382, 526
- Perucho, M., Martí, J. M., Laing, R. A., & Hardee, P. E. 2014, *MNRAS*, 441, 1488
- Perucho, M., Martí, J.-M., & Quilis, V. 2019, *MNRAS*, 482, 3718
- Perucho, M., Martí, J.-M., & Quilis, V. 2022, *MNRAS*, 510, 2084
- Raga, A. C., de Colle, F., Kajdič, P., Esquivel, A., & Cantó, J. 2007, *A&A*, 465, 879
- Ray, T. P., Muxlow, T. W. B., Axon, D. J., et al. 1997, *Nature*, 385, 415
- Reddy, K., Georganopoulos, M., Meyer, E. T., Keenan, M., & Kollmann, K. E. 2023, *ApJS*, 265, 8
- Reipurth, B., Rodríguez, L. F., Anglada, G., & Bally, J. 2004, *AJ*, 127, 1736
- Rieger, F. M. 2019, *Galaxies*, 7, 78
- Rodríguez-Kamenetzky, A., Carrasco-González, C., Araudo, A., et al. 2017, *ApJ*, 851, 16
- Rodríguez-Kamenetzky, A., Carrasco-González, C., Araudo, A., et al. 2016, *ApJ*, 818, 27
- Romero, G. E., Kaufman Bernadó, M. M., & Mirabel, I. F. 2002, *A&A*, 393, L61
- Romero, G. E., Torres, D. F., Kaufman Bernadó, M. M., & Mirabel, I. F. 2003, *A&A*, 410, L1
- Romero, G. E. & Vila, G. S. 2008, *A&A*, 485, 623
- Salvatore, S., Eichmann, B., Rodrigues, X., Dettmar, R.-J., & Becker Tjus, J. 2024, *A&A*, 687, A139
- Sánchez-García, M., García-Burillo, S., Pereira-Santaella, M., et al. 2022, *A&A*, 660, A83
- Scheuer, P. A. G. 1974, *MNRAS*, 166, 513

- Shibata, K. & Uchida, Y. 1986, PASJ, 38, 631
- Shirin T, A., Reville, B., Schween, N. W., Schulze, F., & Kirk, J. G. 2025, MNRAS, 544, L160
- Sironi, L., Petropoulou, M., & Giannios, D. 2015, MNRAS, 450, 183
- Subedi, P., Sonsrtee, W., Blasi, P., et al. 2017, ApJ, 837, 140
- Sudoh, T., Inoue, Y., & Khangulyan, D. 2020, ApJ, 889, 146
- Sunyaev, R., Khabibullin, I., Churazov, E., et al. 2025, arXiv e-prints, arXiv:2510.14938
- Tadhunter, C., Morganti, R., Rose, M., Oonk, J. B. R., & Oosterloo, T. 2014, Nature, 511, 440
- Tavani, M., Bulgarelli, A., Piano, G., et al. 2009, Nature, 462, 620
- Tchekhovskoy, A., Narayan, R., & McKinney, J. C. 2011, MNRAS, 418, L79
- The LHAASO Collaboration, Cao, Z., Aharonian, F., et al. 2025, arXiv e-prints, arXiv:2512.16638
- Tsuji, N., Inoue, Y., Khangulyan, D., et al. 2025, ApJ, 993, L24
- Ulvestad, J. S., Wong, D. S., Taylor, G. B., Gallimore, J. F., & Mundell, C. G. 2005, AJ, 130, 936
- Ustamujic, S., Orlando, S., Bonito, R., et al. 2016, A&A, 596, A99
- Veilleux, S., Cecil, G., & Bland-Hawthorn, J. 2005, ARA&A, 43, 769
- Vila, G. S. & Romero, G. E. 2010, MNRAS, 403, 1457
- Wan, S.-Y., Wang, J.-s., & Liu, R.-Y. 2025, arXiv e-prints, arXiv:2507.02763
- Wang, J., Reville, B., & Aharonian, F. A. 2025, ApJ, 989, L25
- Wang, X. & Loeb, A. 2017, Phys. Rev. D, 95, 063007
- Weaver, R., McCray, R., Castor, J., Shapiro, P., & Moore, R. 1977, ApJ, 218, 377
- Williams, D. R. A., McHardy, I. M., Baldi, R. D., et al. 2017, MNRAS, 472, 3842
- Yan, D.-H., Zhou, J.-N., & Zhang, P.-F. 2022, Research in Astronomy and Astrophysics, 22, 025016
- Yang, R.-z., Li, G.-X., Wilhelmi, E. d. O., et al. 2023, Nature Astronomy, 7, 351
- Yoon, D., Zdziarski, A. A., & Heinz, S. 2016, MNRAS, 456, 3638
- Zdziarski, A. A., Sikora, M., Dubus, G., et al. 2012, MNRAS, 421, 2956
- Zhang, B. T., Kimura, S. S., & Murase, K. 2025, arXiv e-prints, arXiv:2506.20193

Appendix A: Similarities between jets and wind bubbles

It is worth noticing that the jet-cocoon system has the same temporal evolution of an adiabatic wind-blown bubble (Weaver et al. 1977). More specifically, the recollimation shock is the analogous of the wind termination shock, and the jet head and the cocoon expansion evolve like the forward shock in the wind bubble. Such an analogy is to be expected, as both systems are powered by a central source with constant kinetic luminosity. We also notice that the total energy of the jet, $L_j t$, and the one of the swept-up mass, $M_c v_c^2$ have identical scalings with time. Therefore, for the whole period of (steady) activity of the central engine, the cocoon expansion is expected to remain self-similar, regardless of the total mass in the cocoon.

The same scalings obtained in Section 2 arise from solving the momentum and energy conservation equations for the shells, at the jet head ($\dot{M}_{c,h}$) and on the side ($\dot{M}_{c,s}$), driven by the cocoon pressure under self-similar conditions

$$\partial_t[M_{c,h} v_h] = \pi R_c^2 P_c \chi \quad (\text{A.1})$$

$$\partial_t[M_{c,s} v_c] = 2\pi R_c z_h P_c \quad (\text{A.2})$$

$$\partial_t E_c = L_j - \left[\pi R_c^2 v_h \frac{r_{RS}}{(r_{RS} - 1)} + 2\pi R_c z_h v_c \right] P_c, \quad (\text{A.3})$$

where $\chi = \rho_A v_h / P_c$ is the ratio among the ram pressure working on the jet head and the cocoon pressure. R_c and z_h are the cocoon radius and jet head location respectively. While this approach allows to obtain a good estimate of the system scalings ($z_h \sim R_c \sim t^{3/5}$ and $P_c \sim t^{-4/5}$), it does not provide the location of the recollimation shock.

Appendix B: Sink term in the transport equation

In principle, using the formalism presented in this work, it is possible to account also for energy losses or particle escape along the lateral jet surface by introducing a sink term of the form f/τ on the right-hand side of Equation (25).

The inclusion of such a term allow to write the final solution for the distribution function in the same form with the following substitutions:

$$G_0(z, p) \longrightarrow G_0(z, p) + H_0(z, p) \quad (\text{B.1})$$

$$G_1(z, p) \longrightarrow G_1(z, p) + H_1(z, p), \quad (\text{B.2})$$

where

$$H_0(z, p) = \int_0^z dz' f_0(z', p) / \tau(z', p) \quad (\text{B.3})$$

$$H_1(z, p) = \int_z^{z_{\text{esc}}} dz' f_1(z', p) / \tau(z', p). \quad (\text{B.4})$$

Appendix C: Impact of the turbulence cascade in the downstream region – analytic solutions

Given the geometry of the jet, the most natural approximation for the downstream region is the cylindrical one. In this context, the area $A(z)$ becomes a constant. For the flux conservation equation also the downstream speed $u_1(z)$ will remain constant for the whole downstream region.

Now, if the downstream turbulence decays on scales much larger than the jet size, the downstream diffusion coefficient, D_1

can be considered constant and solution can be expressed in the following analytic form

$$f_1(z, p) = f_{\text{sh}}(p) \frac{1 - e^{\mathcal{Y}(z,p) - \mathcal{Y}(z_{\text{esc}}, p)}}}{1 - e^{-\mathcal{Y}(z_{\text{esc}}, p)}} \quad (\text{C.1})$$

$$\mathcal{Y} = \frac{u_1}{D_1(p, z)} (z - z_{\text{sh}}). \quad (\text{C.2})$$

Under the uniform cylindrical approximation, one can show that also the downstream high-energy cutoff function assumes the following simplified form:

$$\Gamma_1(p) = \frac{s}{r} \int_{p_{\text{inj}}}^p \frac{dp'}{p'} \frac{1}{\exp[\mathcal{Y}(z_{\text{esc}}, p)] - 1} \quad (\text{C.3})$$

However, the magnetic turbulence may decay on spatial scales shorter than the jet size and it can be useful to provide the full expressions for such a case. As an example we consider here two possible scenarios: linear decay, i.e $D_1(p, z) = D_0(p)(z/z_{\text{sh}})$, and quadratic decay, $D_1(p, z) = D_0(p)(z/z_{\text{sh}})^2$. For the linear decay, the downstream solution and the cutoff function result in the following expressions

$$f_{1,\text{lin}}(z, p) = f_{\text{sh}}(p) \frac{1 - (z/z_{\text{esc}})^{u_1 z_{\text{sh}}/D_0(p)}}{1 - (z_{\text{sh}}/z_{\text{esc}})^{u_1 z_{\text{sh}}/D_0(p)}} \quad (\text{C.4})$$

$$\Gamma_{1,\text{lin}}(p) = \frac{s}{r} \int_{p_{\text{inj}}}^p \frac{dp'}{p'} \frac{1}{(z_{\text{esc}}/z_{\text{sh}})^{u_1 z_{\text{sh}}/D_0(p)} - 1} \quad (\text{C.5})$$

where $D_0(p)$ is the diffusion coefficient in the immediate downstream of the recollimation shock. We notice that, the functional form of the solution for $D \sim z$ and $D \sim z^0$ are identical with the only exception of the scaling function \mathcal{Y} that shall be replaced by

$$\mathcal{Y}_{\text{lin}} = \frac{u_1 z_{\text{sh}}}{D_0(p)} \ln \left(\frac{z}{z_{\text{sh}}} \right). \quad (\text{C.6})$$

Finally, it is also possible to show that the quadratic decay scenario has identical functional form to the case of constant D_1 , namely Equations (C.1) and (C.3), but with a different scaling function $\mathcal{Y}_{\text{quad}}$ that is modified as in the following expression:

$$\mathcal{Y}_{\text{quad}} = \frac{u_1 z_{\text{sh}}}{D_0(p)} \left(1 - \frac{z_{\text{sh}}}{z} \right). \quad (\text{C.7})$$

Appendix D: Semi-analytic iterative algorithm for the solution of the transport equation

As discussed in Appendix C, the downstream solution, $f_1(z, p)$, depends only on the spectrum at the shock, $f_{\text{sh}}(p)$, and on analytic functions. However, neither the upstream solution nor the shock spectrum admits a simple analytic expression, since they depend in a non-linear way on each other according to Equation (34) and Equation (48), respectively. In particular, the non-linearity is embedded in the term $u_{\text{eff},0}$ for the former, and in Γ_0 for the latter.

In order to find the solutions to Equation (34) and (48) we employ a recursive algorithm. We define as guess functions the expressions characterized by a null implicit part as follows

$$f_{\text{sh}}^{(0)}(p) = \eta_{\text{eff}} \frac{s n_0}{4\pi p_{\text{inj}}^3} \left(\frac{p_{\text{inj}}}{p} \right)^s e^{-\Gamma_0(p)}, \quad (\text{D.1})$$

$$f_0^{(0)}(z, p) = f_{\text{sh}}(p) \exp \left[- \int_z^{z_{\text{sh}}} dz' \frac{u_0(z')}{D_0(z', p)} \right]. \quad (\text{D.2})$$

From the latter expression, at the first step we can compute g_0 , G_0 , $u_{\text{eff},0}$ and Γ_0 from which new expression of f_{sh} and f_0 can be obtained. At the generic step $j + 1$ the solution at the shock and in the upstream read

$$f_{\text{sh}}^{(j+1)}(p) = \eta_{\text{eff}} \frac{sn_0}{4\pi p^3} \left(\frac{p_{\text{inj}}}{p} \right)^s e^{-\Gamma_0(p)} e^{-\Gamma_1^{(j)}(p)}, \quad (\text{D.3})$$

$$f_0^{(j+1)}(z, p) = f_{\text{sh}}(p) \exp \left[- \int_z^{z_{\text{sh}}} dz' \frac{u_{\text{eff},0}^{(j)}(z')}{D_0(z', p)} \right]. \quad (\text{D.4})$$

By comparing $f^{(j+1)}$ with $f^{(j)}$ one can check the convergence, which is typically achieved in a few tens of iterations. At that point, when the convergence is reached, we compute $f_1(z, p)$ following the prescriptions described in Appendix C.

Appendix E: Analytic considerations

For illustrative purposes let us analyze the qualitative properties of the upstream solution assuming a divergence free wind in the jet, namely an idealistic configuration in which $\partial_z[Au] = 0$. For simplicity we also assume a space-independence of the diffusion coefficient. The immediate result of such an assumption is that the functions G_i goes to zero. This reduces the upstream solution, Equation (34), to the well known result of the infinite planar shock:

$$f_0^*(z, p) = f_{\text{sh}}(p) \exp[-(z_{\text{sh}} - z)u_0/D_0(p)]. \quad (\text{E.1})$$

A further consistency check of our solution can be obtained by considering the full spherical expansion, namely when $A(z) \sim z^2$. For the sake of simplicity, let us restrict our attention to the case of adiabatic shocked wind, such that $u_1(z) \sim z^{-2}$. It is straightforward to see that the wind in the region is divergence-free, so that $G_1 = 0$ and $u_{\text{eff},1}(z, p) = u_1(z)$. With a bit of algebra it is possible to show that the function $\mathcal{I}(z, p)$ assumes the following analytic expression

$$\mathcal{I}^*(z, p) = \frac{1}{u_1 z_{\text{sh}}^2} \{1 - \exp[-\mathcal{Y}^*(z, p)]\} \quad (\text{E.2})$$

$$\mathcal{Y}^*(z, p) = \frac{u_1 z_{\text{sh}}}{D_1(p)} \left(1 - \frac{z_{\text{sh}}}{z}\right). \quad (\text{E.3})$$

Substituting the latter expression in the downstream solution one obtains the following result:

$$f_{1,\text{sph}}^*(z, p) = f_{\text{sh}}(p) \frac{1 - e^{\mathcal{Y}^*(z,p) - \mathcal{Y}^*(z_{\text{esc}},p)}}{1 - e^{-\mathcal{Y}^*(z_{\text{esc}},p)}} \quad (\text{E.4})$$

which coincides with the solution provided in Morlino et al. (2021) for the case of the adiabatic stellar cluster wind.